Title

Geology of the Alarcon Rise, Southern Gulf of California

Journal

Geochemistry Geophysics Geosystems, 19(3)

ISSN

1525-2027

Authors

Clague, David A
Caress, David W
Dreyer, Brian M
et al.

Publication Date

2018-03-01

DOI

10.1002/2017gc007348

Peer reviewed

AGU PUBLICATIONS

Geochemistry, Geophysics, Geosystems

RESEARCH ARTICLE

10.1002/2017GC007348

Geology of the Alarcon Rise, Southern Gulf of California

David A. Clague[1], David W. Caress[1], Brian M. Dreyer[2], Lonny Lundsten[1], Jennifer B. Paduan[1], Ryan A. Portner[3], Ronald Spelz-Madero[4], Julie A. Bowles[5], Paterno R. Castillo[6], Rigoberto Guardado-France[4], Morgane Le Saout[1], Julie F. Martin[7], Miguel A. Santa Rosa-del Río[4], and Robert A. Zierenberg[8]

[1]Research Division, Monterey Bay Aquarium Research Institute, Moss Landing, CA, USA, [2]Earth and Planetary Sciences, University of California at Santa Cruz, Santa Cruz, CA, USA, [3]Geology Department, San Jose State University, San Jose, CA, USA, [4]Facultad de Ciencias Marinas, Universidad Autónoma de Baja California, Ensenada, BC, México, [5]Geosciences Department, University of Wisconsin at Milwaukee, Milwaukee, WI, USA, [6]Geological Research Division, Scripps Institution of Oceanography, La Jolla, CA, USA, [7]School of Natural Sciences, California State University at Monterey Bay, Seaside, CA, USA, [8]Earth and Planetary Sciences, University of California at Davis, Davis, CA, USA

Key Points:
- Sampling of the Alarcon Rise neovolcanic zone and adjacent Pescadero and Tamayo transform faults was guided by 1 m resolution bathymetry
- The shallowest, but not central, part hosts four active hydrothermal fields and the youngest, hottest, highest effusion rate lava flows
- Basaltic andesite, andesite, dacite, and rhyolite lavas at the north end formed by crystal fractionation, mixing, and assimilation

Supporting Information:
- Supporting Information S1
- Figure S1
- Table S1
- Table S2

Correspondence to:
D. Clague,
clague@mbari.org

Citation:
Clague, D. A., Caress, D. W., Dreyer, B. M., Lundsten, L., Paduan, J. B., Portner, R. A., et al. (2018). Geology of the Alarcon Rise, southern Gulf of California. *Geochemistry, Geophysics, Geosystems*, *19*. https://doi.org/10.1002/2017GC007348

Received 20 NOV 2017
Accepted 13 FEB 2018
Accepted article online 26 FEB 2018

Abstract Meter-scale AUV bathymetric mapping and ROV sampling of the entire 47 km-long Alarcon Rise between the Pescadero and Tamayo transforms show that the shallowest inflated portion of the segment hosts all four active hydrothermal vent fields and the youngest, hottest, and highest effusion rate lava flows. This shallowest inflated part is located ~1/3 of the way between the Tamayo and Pescadero transforms and is paved by a 16 km^2 channelized flow that erupted from 9 km of en echelon fissures and is larger than historic flows on the East Pacific Rise or on the Gorda and Juan de Fuca Ridges. Starting ~5 km south of the Pescadero transform, 6.5 km of the Alarcon Rise is characterized by faulted ridges and domes of fractionated lavas ranging from basaltic andesite to rhyolite with up to 77.3 wt % SiO_2. These are the first known rhyolites from the submarine global mid-ocean ridge system. Silicic lavas range from >11.7 ka, to as young as 1.1 ka. A basalt-to-basaltic andesite sequence and an andesite-to-dacite-to-rhyolite sequence are consistent with crystal fractionation but some intermediate basaltic andesite and andesite formed by mixing basalt with dacite or rhyolite. Magmatism occurred along the bounding Tamayo and Pescadero transforms as extensive channelized flows. The flows erupted from ring faults surrounding uplifted sediment hills inferred to overlie sills. The transforms are transtensional to accommodate magma migration from the adjacent Alarcon Rise.

Plain Language Summary This study combines 1 m resolution bathymetry collected using an autonomous underwater vehicle, with chemical compositions of precisely located lava samples and ages of lava flows determined from short sediment cores collected using a remotely operated vehicle. The objective was to determine the history of an entire 47 km long segment of the global mid-ocean ridge system. The ridge segment studied is named the Alarcon Rise and is located at the mouth of the Gulf of California. The Rise is bounded to the north and south by strike-slip faults that offset the Rise from adjacent segments of the spreading ridge system. Such faults are usually thought to be parallel to the direction of seafloor spreading, but these have an oblique component to their movement that makes space for magma to be injected along the faults where it uplifts hills of sediment and sometimes erupts. Most lavas erupted along mid-ocean ridges are basalts, but some highly unusual silica-rich lavas were identified by their rough surface texture and sampled. These lavas include the most silica-rich ones found along the entire global submarine mid-ocean ridge system. They formed, not by melting of nearby continental crust, but from common basalt by extreme amounts of crystallization of minerals, leaving a small volume of remaining high-silica magma. The complete mapping and closely spaced sampling along the Rise show that old ideas indicating a central point of magma delivery from the underlying mantle for each ridge segment followed by shallow transport of the magmas along the ridge are supported by the central distribution of (1) hydrothermally active sites, (2) the youngest, hottest, most fluid lava flows, and (3) the most voluminous lava flows that accumulate to form the shallowest portion of the ridge segment. The study shows how magmas are transported at shallow depths along the ridge and even around the corners in the adjacent faults.

1. Introduction

Many parameters are proposed to vary systematically along segments of fast spreading mid-ocean ridges from a magmatically robust midsegment to distal transform faults or second-order discontinuities (see summary in Macdonald, 1998). Some parameters are at their maxima midsegment, including cross-sectional area of the ridge axis, MgO content and eruption temperature of the lavas, presence of an axial magma chamber, hydrothermal activity, and width of fissures. Other parameters are at their minima midsegment including axial depth, crustal magnetization, mantle Bouguer gravity anomaly, average lava age, abundance of fissures, and near axis scarp height. The distribution of these parameters along ridge segments is generally not well constrained. Highly evolved mid-ocean ridge lavas (andesites and dacites) occur preferentially near ridge segment ends (e.g., Wanless et al., 2010 and references therein) due to a "cold-edge effect." Not only do ridges vary along strike, but also across-strike. Channelized lava flows, for example, are emplaced up to 3 km from the fast spreading East Pacific Rise (EPR; e.g., Soule et al., 2005), and ~2 km at the intermediate-spreading Endeavour segment of the Juan de Fuca Ridge (Clague et al., 2014), but a high-resolution study at the intermediate-spreading Galapagos Rise (Colman et al., 2012) did not find emplacement of long flows off axis. Off-axis distribution of flows has important implications for how the ocean crust is constructed (e.g., Perfit & Chadwick, 1998), but the parameters, such as lava viscosity, that control flow distribution, are poorly understood. Some transform faults, including Tamayo transform (TT; Kastens et al., 1979; Macdonald et al., 1979), were described as "leaky" due to ridge reorientation causing extension (transtension) across the transform but rarely have lava flows been mapped on them.

Macdonald's model links tectonic, magmatic, and hydrothermal processes at fast spreading mid-ocean ridges to suggest that magma supply is focused at the segment scale, with mantle upwelling zones linked to segmentation. Studies that informed this model combined ship-based mapping data, multichannel seismic reflection profiling, gravity and magnetic surveys, and submersible dives for direct observations and sampling. Other studies have utilized high-resolution multibeam and side-scan sonar data (e.g., Chadwick et al., 2013; Clague et al., 2013, 2014; Ferrini et al., 2007; Fornari et al., 2004, 2012) to study parts of ridge segments, but none have previously mapped and sampled an entire ridge segment. To evaluate if the same linkages are observed at higher data density and occur at lower spreading rates, the intermediate-rate Alarcon Rise (AR) in the southern Gulf of California (Figure 1) was mapped at 1 m lateral resolution and densely

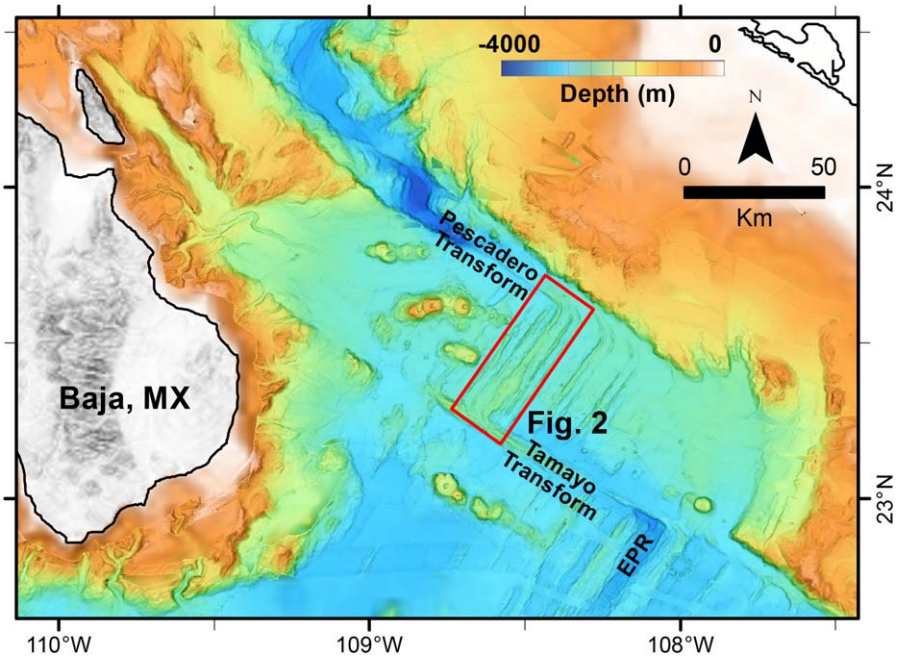

Figure 1. Regional map of the southern Gulf of California showing location of Alarcon Rise in the red box that is the extent of Figure 2. The bathymetry is a merge of ship-collected multibeam data and satellite altimetry. The Pescadero and Tamayo transforms and the axis of the East Pacific Rise (EPR) are labeled.

sampled. The AR is only ~50 km from transform-to-transform, making it logistically feasible to map at high-resolution using AUVs and to observe and to sample at high density using an ROV. The data are used to evaluate these long-standing ideas (e.g., Macdonald, 1998; Macdonald et al., 1991) about the distribution of active hydrothermal vents, lava compositions, and lava flow ages along ridge segments; flow ages away from the axis of the ridge; the formation of highly evolved lavas on mid-ocean ridges, and extrusion and intrusion along transform plate boundaries.

Features that were recognized, observed, and sampled based on the 1 m resolution maps include (1) an extensive young channelized flow that underlies three of four active hydrothermal fields and is adjacent to the fourth, (2) a km-scale rhyolite dome and associated smaller rhyolite, dacite, andesite, and basaltic andesite flows on the northern AR, (3) widespread intrusive and extrusive magmatism on the Pescadero transform (PT) and the TT, and (4) repaving of off-axis regions by flows that extend multi-km from the ridge axis.

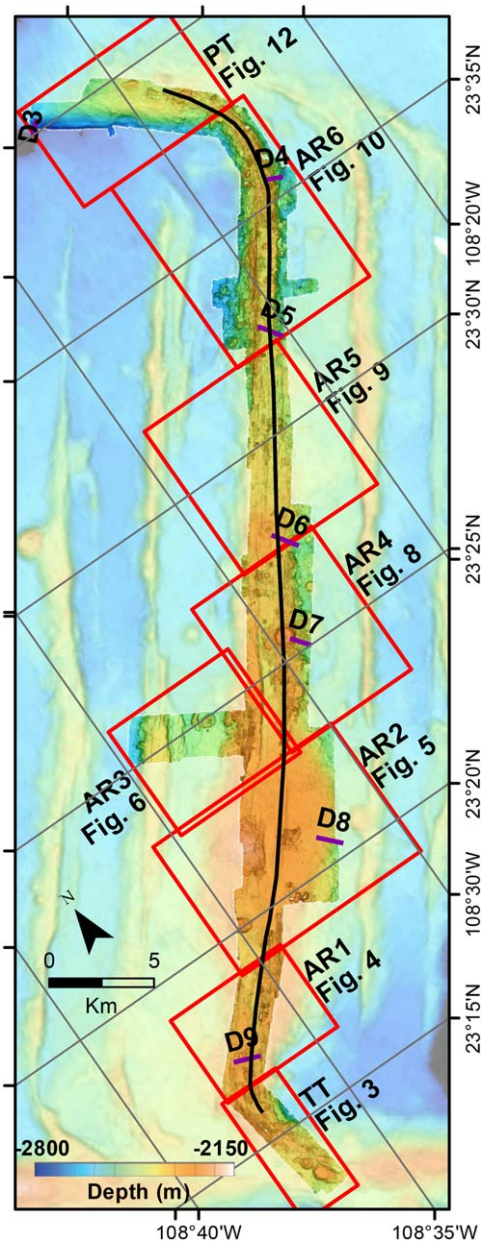

Figure 2. Map showing Alarcon Rise AUV 1 m resolution bathymetric coverage over faded ship-based multibeam bathymetry. Red boxes define regions illustrated in subsequent maps and discussed in the text. TT, Tamayo transform; AR1 to AR6, south to north sections of Alarcon Rise along the axis; PT, Pescadero transform. Black line indicates the center of the neovolcanic zone. Labeled purple lines show the location of dredges from Castillo et al. (2002).

2. Geological Setting and Previous Work

The AR, the northernmost bare-rock segment of the EPR, is located adjacent to the southeastern tip of Baja California (Figure 1). It is bounded by the TT to the south and the PT to the north and has a full-spreading rate of about 4.9 cm/yr (DeMets et al., 2010). To the north, spreading separating the North American and Pacific plates takes place in a series of sediment covered basins offset by long transform faults, with the northernmost being the San Andreas fault. AR experienced 350 km of continental crustal extension before seafloor spreading that began 2–3 Ma produced ~135 km of oceanic crust (Lizarralde et al., 2007). The AR was previously sampled by 6 dredges in 1998 (Castillo et al., 2002) that recovered andesite and T-MORB from near the Pescadero transform to evolved to primitive (6.4–8.0% MgO) N-MORB from the five southern dredges (Figure 2). Geophysical and deep-tow surveys of the TT (Kastens et al., 1979; Macdonald et al., 1979) suggested that the transform was "leaky" with intrusion of mantle diapirs and extrusion of lava. The AR is characterized by alternating ridges (abyssal hills) and flat-floored valleys away from the axial high that are similar to those identified by Kappel and Ryan (1986) to infer cyclic changes from magmatism that produces the ridges to tectonism that produces the intervening valleys.

3. High-Resolution Mapping and Targeted Sampling

In 2003, two remotely operated vehicle (ROV) *Tiburon* dives searched for hydrothermal vent communities on AR, focusing on a region where deep-tow surveys by Castillo et al. (2002) detected water column anomalies.

In the ensuing years, MBARI developed the autonomous underwater vehicle (AUV) *D. Allan B.*, which collects multibeam and side-scan sonar data, and chirp subbottom seismic data at high resolution (Caress et al., 2008). The bathymetric data resolve individual chimney structures and detailed lava flow morphologies (Clague et al., 2013, 2014; Clague & Paduan, 2009; Jamieson et al., 2013, 2014). The AUV was deployed for nine missions on AR in 2012 to map a roughly 2 km-wide swath of the neovolcanic zone between the PT and the TT (Figure 2). The AUV maps guided eight subsequent ROV *Doc Ricketts* dives along the AR for targeted geological sampling and observations. MBARI returned in 2015 and expanded coverage during eight AUV

surveys. ROV *Doc Ricketts* then completed eight dives between the TT and the PT. The area along and near AR with 1 m resolution bathymetric coverage is ~164 km^2. The AUV mapping data are archived and available in Caress et al. (2018) at IEDA.

Here we present the geology of the AR as deduced from the maps and sampling. We use flow-scale morphological terminology (Clague et al., 2017; modified from Chadwick et al., 2013) instead of visual scale lava morphology terminology. We use "channelized flow" to describe flows with proximal sheet flow channels, lobate flow margins (with or without pillars), and distal pillow lobes. We use "hummocky flows" to describe mounds or coalesced mounds of mainly pillow lava, with or without lava drain-back features (collapses), or small lava ponds at their summits.

4. Methods

The MBARI Mapping AUVs collect sonar data from an altitude of 50 m to achieve 1 m resolution bathymetry (file size limits the maps presented here to 2 m grids made from the 1 m data) and up to ~50–100 m subbottom seismic penetration (see Caress et al., 2008 and supporting information S1 for technical details about the AUV and data processing). Where subbottom chirp detected sediment, sediment is inferred to be >~2–3 m thick. Full penetration is about 0.07 s two-way travel time (TWTT), or about 70 m, so thicker sediment is not fully imaged.

Volcanic glasses were analyzed using a Cameca SX-100 electron microprobe at the University of California at Davis using natural and synthetic standards (supporting information Table S1). Twelve samples from Castillo et al. (2002) were reanalyzed for comparison and their remaining glasses were adjusted to account for an adjustment in the MgO value from 6.72 to 7.07 wt % in standard VG2. Sample preparation and standardization are presented in supporting information S1. Values presented in the text are normalized to 100 wt % totals for plotting.

Foraminifera recovered from the base of push cores collected by the ROV were radiocarbon dated. Details of subsampling, dating, and calibration of the radiocarbon ages are in Clague et al. (2013, 2014) and supporting information S1. Ages are reported in the text in ka (relative to 1950 C.E.), rounded to the nearest tenth of a ka, for ages >1 ka and in year for those <1,000 years. Age data are in supporting information Table S2.

5. Results

5.1. Mapping an Entire Ridge Segment at High Resolution

5.1.1. Introduction

The 17 AUV surveys provide full coverage of the neovolcanic zone of the ridge segment and the intersections with the TT and the PT (Figure 2). Extensive channelized flows in the southern third of the ridge required broader coverage than elsewhere along the segment, but our mapping still did not cover these flows in their entirety. One survey was completed on the northwest side and perpendicular to the axis. For descriptive purposes, the ridge and adjacent transforms are divided into eight regions (Figure 2) starting at the southern end at TT and progressing to the north through ridge axis regions AR1 to AR6 and ending with the northern map of PT. The locations of 19 ROV dives on and near the axis from 2003, 2012, and 2015, and of 29 wax-tipped rock cores recovered in 2012 and 2015 are shown on subsequent maps, with glass analyses of lava samples color coded by MgO content, ages of the base of cores color coded by age brackets, and locations of active and inactive hydrothermal chimneys also plotted. We have largely refrained from mapping individual flow boundaries as much of the ridge is constructed of hummocky flows that can erupt as disconnected mounds, even when from the same eruption (Yeo et al., 2013).

5.1.2. Morphology of the AR and Transforms

The following sections are based on high-resolution bathymetry, glass compositions, sediment cover detected by the AUV chirp subbottom sonar, sediment cores, and minimum radiocarbon ages of underlying flows. The fine-scale segmentation of the ridge is described in Le Saout et al. (2016) and the faulting and structure of the ridge by Spelz et al. (2012).

At the southeast end of TT, several sediment hills stand above, and are surrounded by channelized lava flows (Figure 3). The two largest hills are 1,100 by 750 m and 500 by 600 m across and 80–100 m tall (Figure 3A)

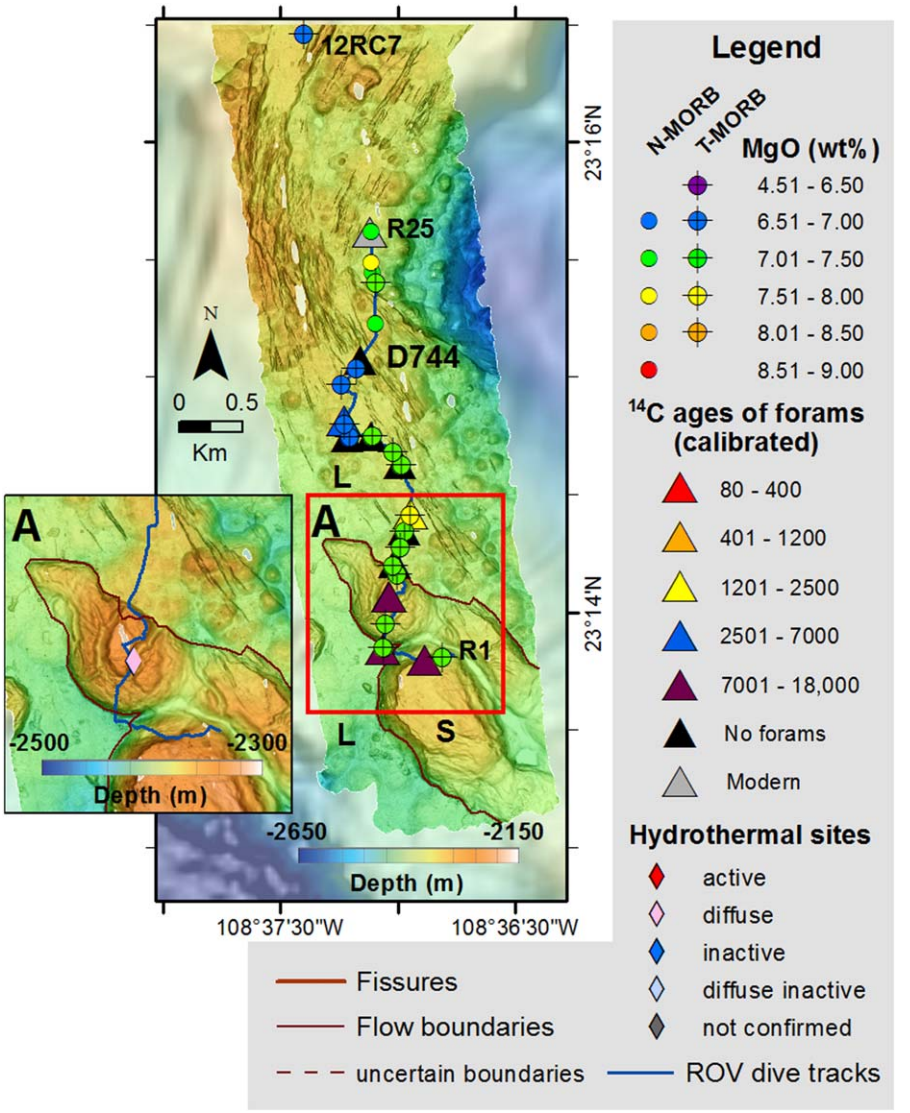

Figure 3. TT map with ROV dive D744 track, lava samples from dive (with first and last rock samples labeled as R1 and R25) and wax-tip rock core 12RC7 color coded by MgO content and with different symbols for N-MORB and T-MORB. Push cores are color coded by radiocarbon age of basal slice. The legend defines symbols used in all subsequent maps except Figures 10 and 19, which also divide the lavas by lithology. Inset A, indicated by red box, shows the location of a low-temperature hydrothermal seep site on a sediment hill. This hydrothermal site was not identified in the AUV bathymetry. Lava flows (L) cover the seafloor west and north of the flow boundary line whereas thick sediment (S) characterizes the seafloor in the southeast portion of the map.

and the top surfaces are smooth or deeply cracked poorly lithified sediment, or steeply tilted sheet flows. At the NW end, where TT turns to become the Alarcon Rise, the transform consists of numerous hummocky flows consisting of pillow lava, most cut by faults and fissures except in an area east of the intersection that is relatively undisrupted. Faults and fissures are parallel to the AR at the northern end but rotate sharply to be nearly parallel to the TT at 23°15.5′N.

The 6.5 km-long AR1 has a shallow axial graben (Figure 4). At the southern end on the west side, faults are rotated toward the trend of the TT. Lava flows are hummocky flows of pillow lava that range from having no fissures and faults to being highly disrupted. A dense network of fissures located near the SE side of the axis, especially in the northern part of the region, is inferred to mark the present spreading axis (Le Saout et al., 2016).

The broadly inflated 10.2 km AR2 (Figure 5) is the shallowest section of the axis and is mainly paved by extensive channelized flows. The youngest of these flows, and probably of the AR, is identified as such in

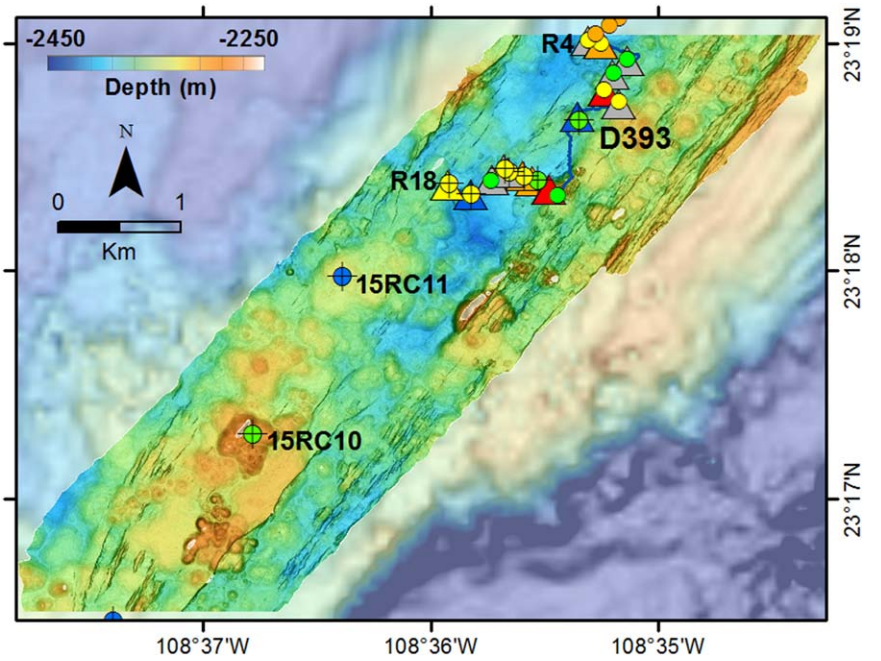

Figure 4. AR1 map with dive D393 track, lava samples (with first and last lava samples labeled R4 and R18), rock cores 15RC10 and 15RC11, and dated cores are symbolized as in Figure 3. There are no identified hydrothermal chimneys.

the AUV maps because its distal portions overrun other flow channel systems, no subsequent channels or hummocks have erupted on top of it, it is not cut by any faults or fissures wider than 1 m (the resolution of the AUV bathymetry) except for the fissure system through which it erupted, and it has the least sediment

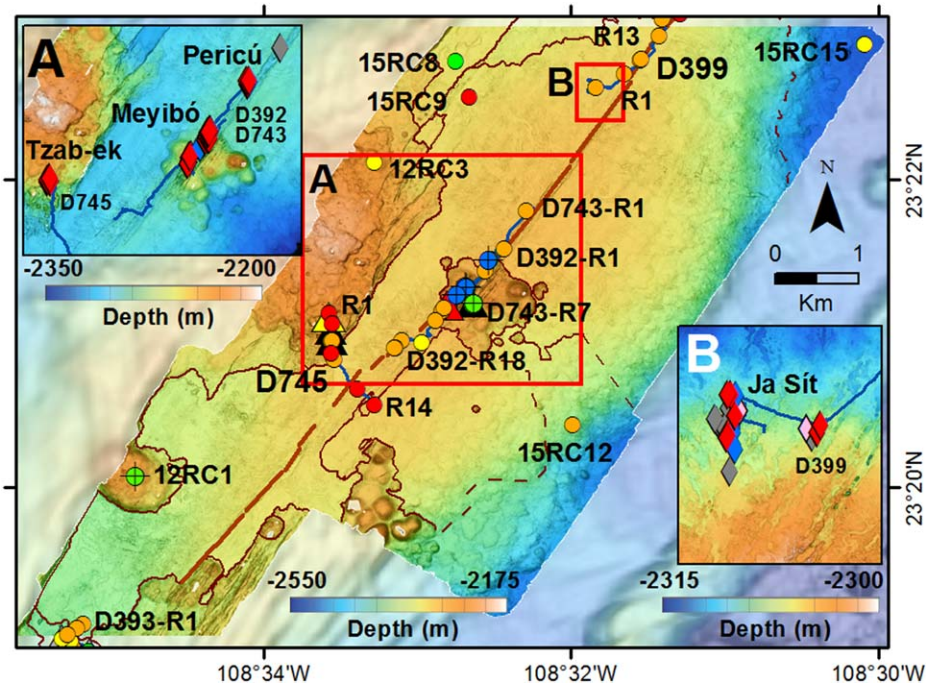

Figure 5. AR2 map with dive tracks for D392, D743, D745 and the beginning of D393 and D399. Lava samples from ROV dives (with first and last rock samples labeled); rock cores 12RC1, 12RC3, 15RC8, 15RC9, 15RC12, and 15RC15; and dated cores are symbolized as in Figure 3. The red boxes A and B show extent of insets showing active and inactive chimneys at the active vent fields with Tzab-ek, Meyibó, and Pericú in A and Ja Sít in B, symbolized as in Figure 3.

cover of the ROV-observed flows, being far too thin to core. It is the southernmost channelized flow on AR and covers at least 15.9 km^2 (albeit with uncertain contacts on NE margin, Figures 5 and 6). It erupted from a series of at least 14 en echelon right-stepping fissures extending for ~9 km (Figure 5). The fissures cut through a cluster of older mound to low-cone shaped hummocky flows of pillow lava roughly in the center and at the shallowest part of the fissure system. Where the eruptive fissures cut through the hummocky flows, the total extension is about 100 m. The flow has numerous well-developed channels (Figure 6A) that transported lava away from the fissure system. To the northwest and southwest, the flow was impounded by fault scarps on the west side of the axis and flowed around a 700 m diameter, 110 m tall, flat-topped cone (Figure 6). Where it ponded against the cone and faults, it left 6 m tall "bathtub" rings (arrows in Figure 6B) after the lava drained. The distal southwest end of the flow has slightly elevated channels

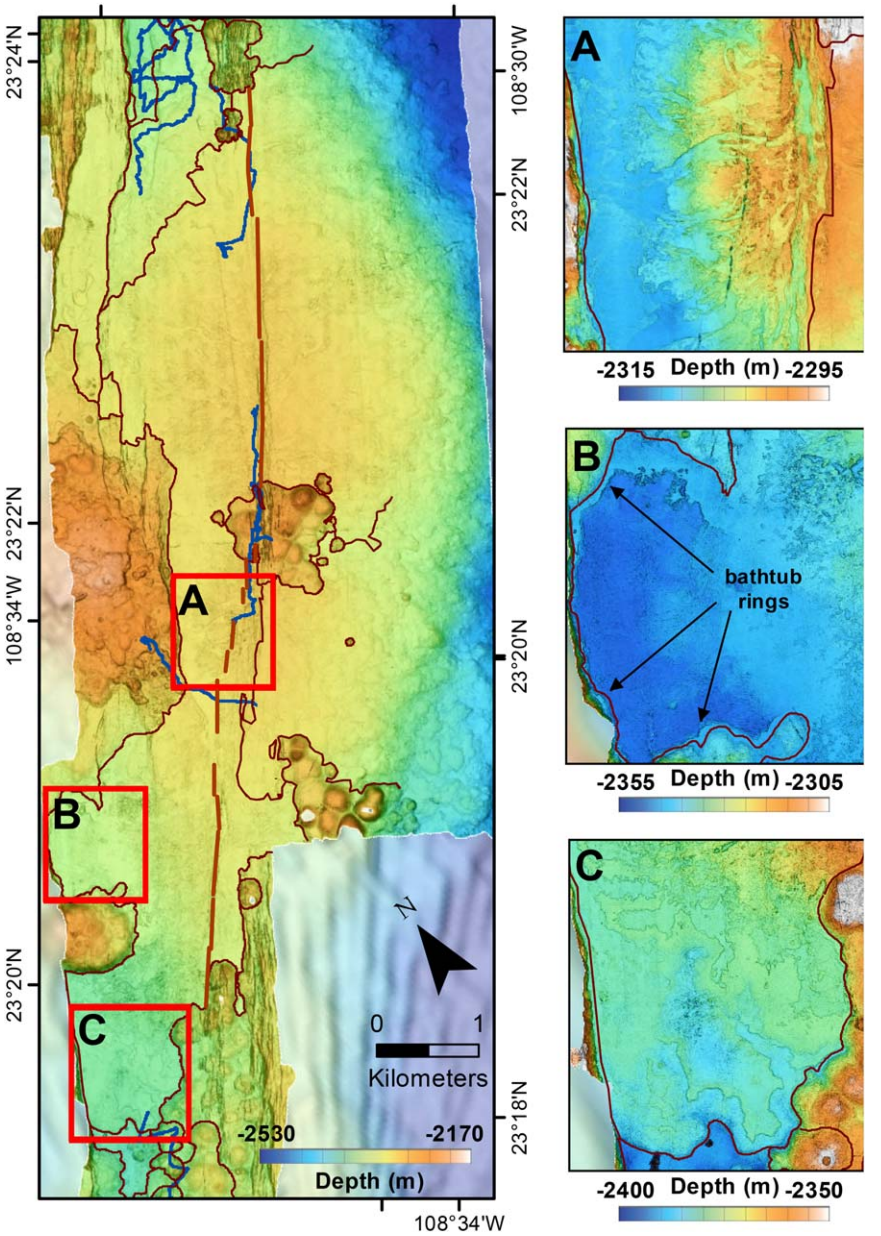

Figure 6. The extensive channelized flow in AR2 (rotated map) with three insets to illustrate details of flow emplacement. Inset A shows the well-developed channel system near the eruptive fissures. Inset B shows lava that ponded against a fault and then partially drained leaving a narrow bathtub ring (pale blue against deep blue) around the margins of the lava pond. Inset C shows internal and overlapping flow lobes with slightly inflated margins and flow interiors that subsided as the flows spread out.

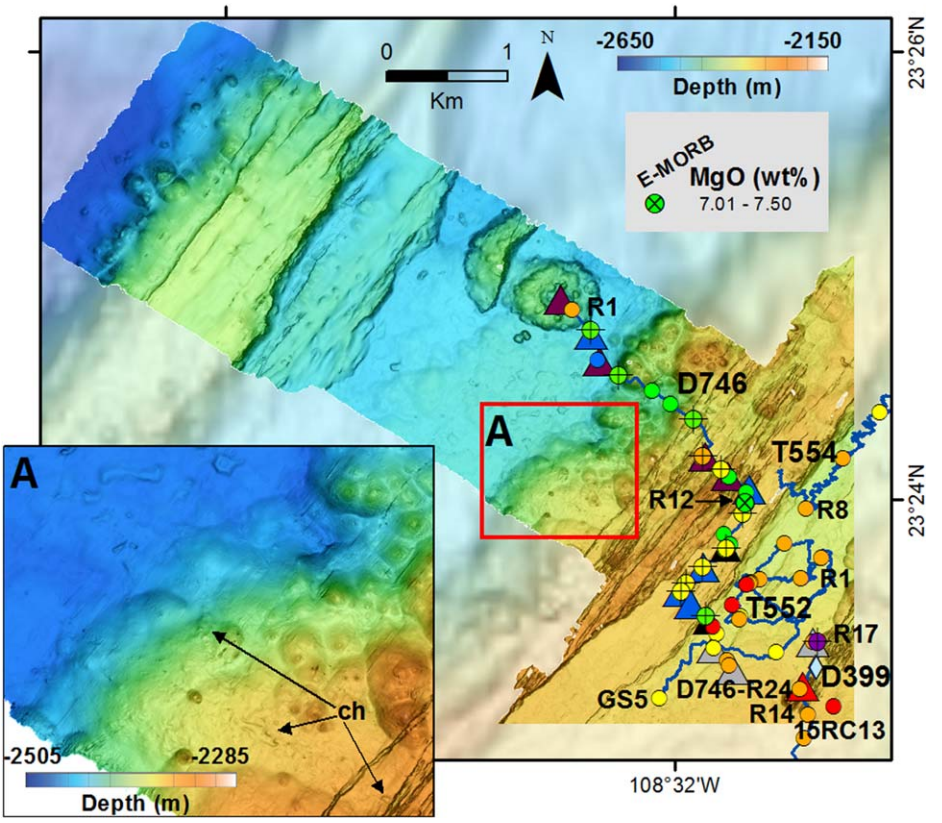

Figure 7. AR3 map with tracks for dives T552 and D746 and the ends of dives T554 and D399. Lava samples from ROV dives (with first and last rock samples labeled), rock core 15RC13, and dated cores symbolized as in Figure 3. A single diffuse hydrothermal site (not identified in the AUV data) is shown as a light blue diamond. Inset A shows a channelized flow that originated at the fissure swarm in the SE corner of the inset and advanced down a channel system (ch) to supply flows with tumulus and pillowed margins that paved over the valley to the NW.

surrounded by lobate and pillowed flow margins (Figure 6C). This inflated shallowest AR2 section of the axis is not centrally located within the ridge segment, but is instead about 1/3 of the distance from TT to PT (Figure 2).

AR3 extends perpendicular to the spreading axis, and was chosen for mapping to generate a cross section of off-axis terrain. It consists of a series of fault-bounded ridges or abyssal hills constructed during earlier magmatically robust periods and flat-floored valleys parallel to the axis (Figure 7) that become progressively more sedimented away from the axis. The active axis is on the east edge of a graben and is characterized by numerous fissures that cut through hummocky flows in a ~400 m wide zone. To the NW, channelized flows in the graben are largely uncut by faults and fissures until a large fault on the WNW margin of the graben. These lavas may have flowed along the western bounding fault to the ENE from eruptive fissures located in AR2 but buried by subsequent channelized flows.

The first terrace west of the axial graben consists mainly of channelized flows that are cut by rare faults on the ESE part, and hummocky flows that are cut by abundant faults and fissures on the WNW portion. The outer slope of the ridge consists of low-to-moderate-relief hummocky flows and is uncut by faults and fissures.

The 600 m diameter, 55 m tall cone-shaped hummocky flow in the valley WNW of the axis has a summit crater 250 m across and 45 m deep, so the bottom of the crater is within ~10 m of the surrounding surface. The half-moon cone-shaped hummocky flow immediately WNW was bisected by spreading and the eastern half is located ESE of the ridge (it can be seen in the ship bathymetry of Figure 2 straddling the center of the southern boundary of the AR4 red box). Channelized flows that transition to lobate and inflated lobes with pillowed margins occur as far as 4 km WNW of the axis (Figure 7A). These channelized flows have flow directions to the NW to WNW and some can be traced upslope to the ESE. There are no faults or fissures

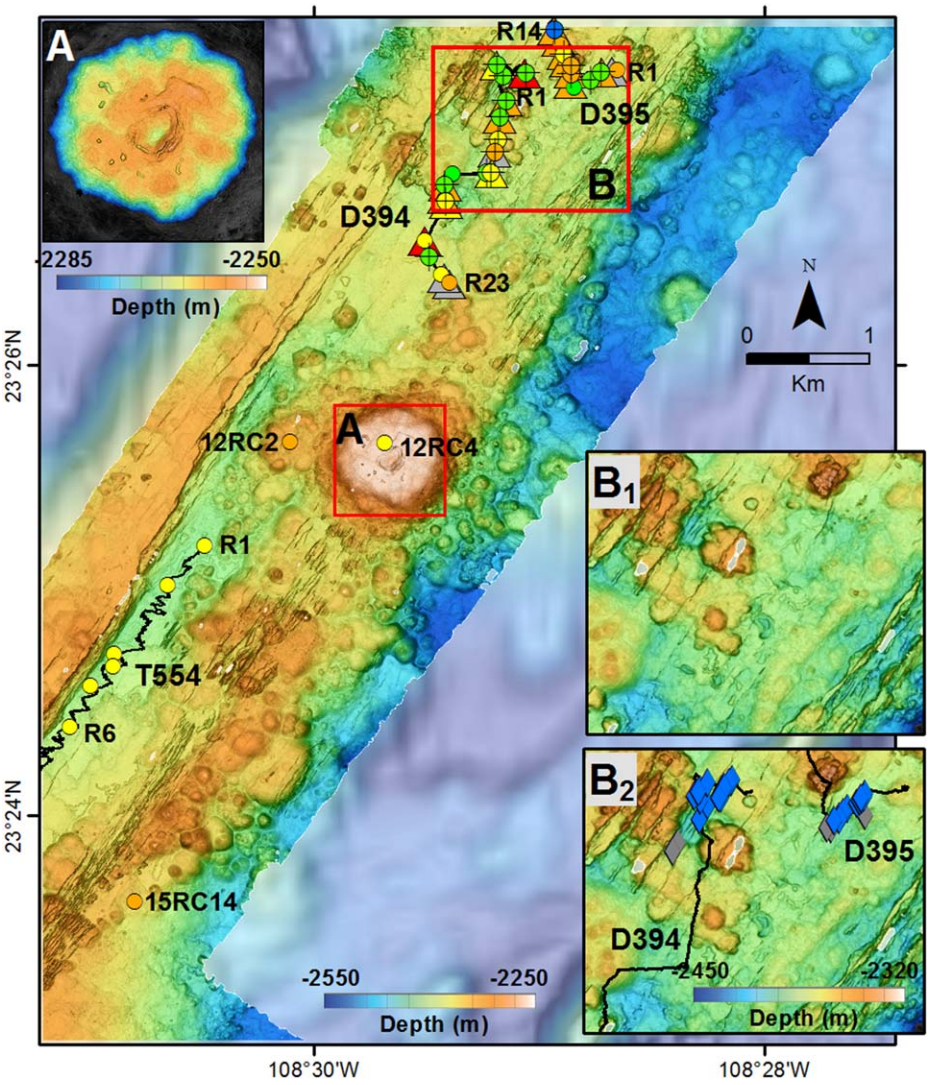

Figure 8. AR4 map with tracks for dive D394 and the first parts of D395 and T554. Lava samples from ROV dives (with first and last rock samples labeled), rock cores 12RC2 and 12RC4, and dated cores symbolized as in Figure 3. Inset A of the top of the "flat-topped" cone shows that the summit consists of a ring of low pillow mounds surrounding a central partly drained lava pond. Black is deeper than the 35 m range of the color ramp. Inset B shows an area with numerous inactive chimneys. The processed merged data used to identify chimneys are shown with no interpretation (inset B_1) and with the chimneys classified as inactive based on ROV observations or unknown activity (inset B_2).

between about 2 and 4.5 km WNW of the axis. Flow morphologies farther WNW from the axis are obscured by sediment cover, although faults and fissures are common and several small hummocky flows can be identified on the WNW slope of the westernmost abyssal hill.

The 10 km-long AR4 (Figure 8) has a central graben floored by young channelized flows. A network of fissures and a 1.2 km-diameter flat-topped cone (Figure 8A) on the SE margin of the graben define the current axis of spreading in the southern half of the region. This cluster of fissures is aligned with the wide fissure that fed the young channelized flow in section AR2 (Figure 6). Two flows about the fault on the NW side of the graben in AR4: the northern one is a hackly channelized flow and the southern one is a channelized flow that continues into AR3. An older channelized flow underlies the young channelized flow that dominates AR2 at the southern end of the axial graben. These flows erupted from fissures along the east side of the graben and flowed WNW before spreading laterally along the fault that bounds the northwest side of the graben. Hummocky flows and rarer, small channelized and inflated flows (Figure 8B) occur in the northern half of AR3. The summit of the 1.2 km-diameter, 110 m tall, nearly flat-topped cone has a shallow

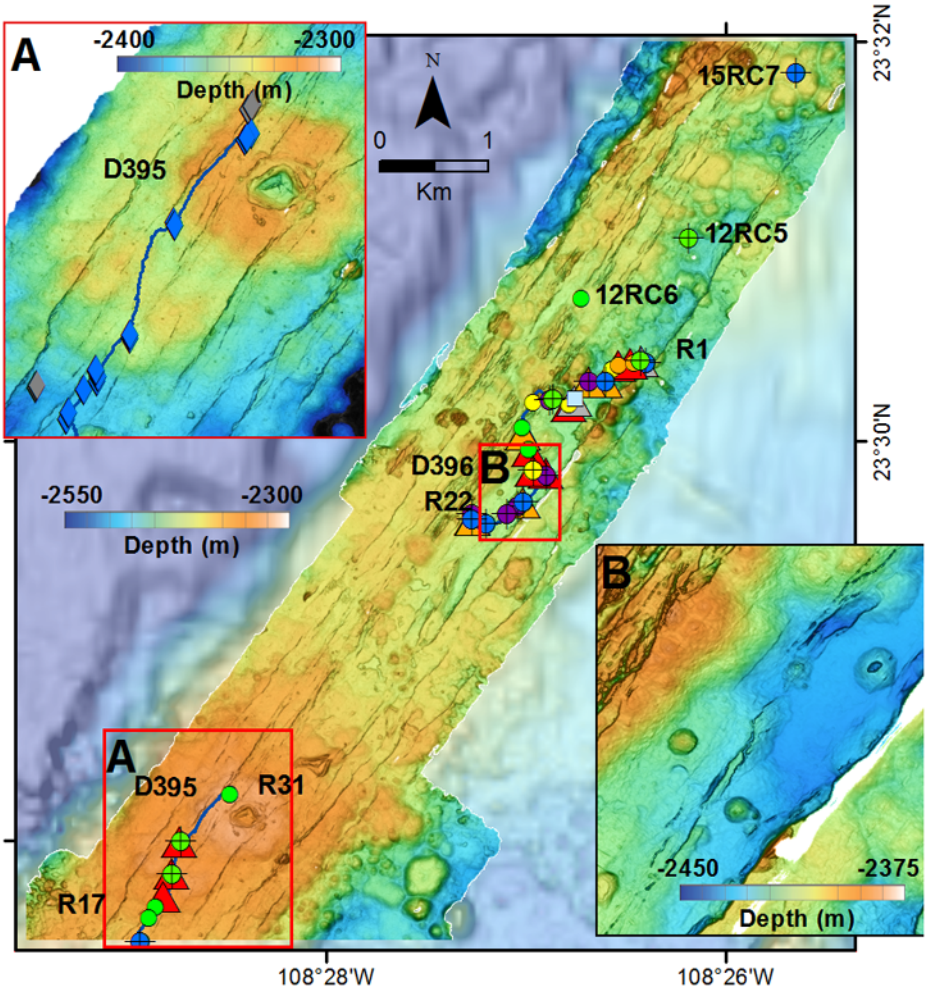

Figure 9. AR5 map with dive D396 and the end of D395 tracks. Lava samples from ROV dives (with first and last rock samples labeled); rock cores 12RC5, 12RC6, and 15RC7; and dated cores symbolized as in Figure 3. Red boxes show the extents of insets A and B. Inset A shows a low-relief faulted lava shield discussed in the text and the locations of inactive chimneys symbolized as in legend to Figure 3. Inset B shows four small steep-sided hummocky mounds made of pillows among low-relief hummocky flows, also constructed of pillows. The northeastern steep mound has a summit crater.

(~12 m deep) drained lava lake about 150 by 200 m across encircled by low levees (Figure 8A) and surrounded by a ring of low mounds. The cone is not cut by fissures or faults.

AR5 (Figure 9) is ~10 km long and includes a low shield volcano near the southern end that is ~2.6 km in diameter, but only 25 m tall (Figure 9A). This shield is cut by ridge-parallel fissures and surmounted by a 220 m diameter, 30 m deep summit crater, indicating that the crater collapsed below the level of the preexisting surface below the shield. In general, hummocky flows dominate the western part of the axis and channelized flows the eastern half, although several hummocky flows form steep-sided small pillow mounds among the channelized flows with lobate to pillowed margins (Figure 9B). Despite their small size (<100 m across), the northeasternmost of these steep pillow mounds has a summit crater (Figure 9B), consistent with a molten core that drained late in the formation of the mound. The northernmost channelized flows on AR are located about 800 m south of the northern end of AR5 at ~23°31′N. Channelized flows occur along ~29 km of the axis from ~23°19′N on AR2 to here, with those in AR5 partly buried by hummocky flows, smaller, and more widely spaced than those in AR2.

AR6 (Figure 10), the next ~11 km section to the north, is characterized by a highly faulted, axial ridge extending from a rough dome 600 by 450 m by 80 m tall (Figure 10A). The rough terrain is comprised

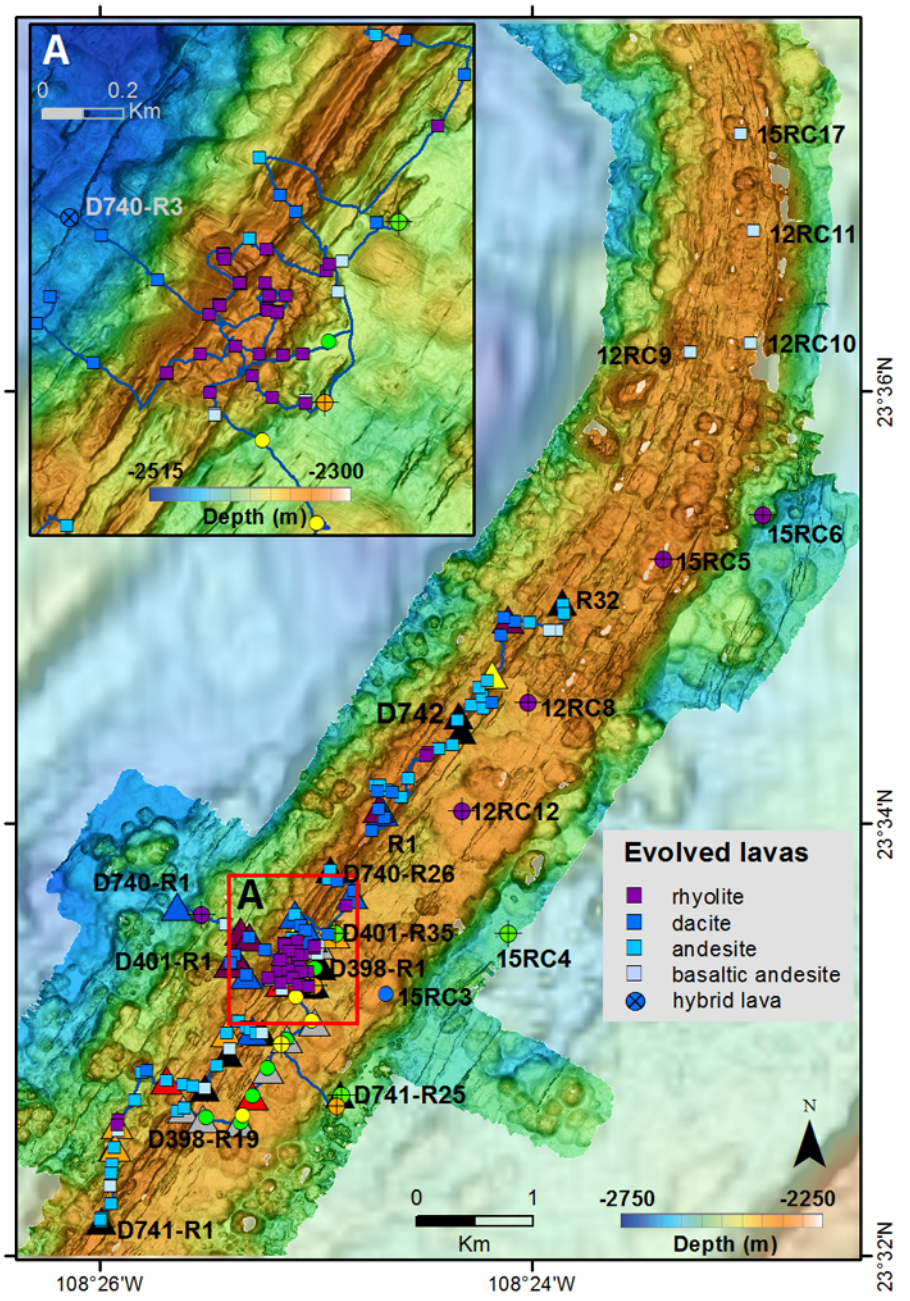

Figure 10. AR6 map with tracks for dives D398, D401, D740, D741, and D742. Lava samples from ROV dives and rock cores 12RC8 to 12RC12, 15RC3 to 15RC6, and 15RC17 symbolized by lithology as in the legend for lavas more evolved than basalt and as in Figure 3 for MORBs. Dated cores are symbolized as in Figure 3. The red box shows the area of inset A that shows a rhyolite dome onlapped from the east by younger MORB and evolved MORB. The inset also shows a smaller rhyolite outcrop to the north, four separate dacite outcrops, and four outcrops of andesite and basaltic andesite. MORB hybrid lava D740-R3, discussed in the text, is labeled in the inset.

exclusively of evolved lavas that crop out for 5.9 km centered on the large dome. Two smaller, similarly textured domes are 1.7 km SSW and 2.0 km NNE along the horst from the central dome (see below). High-relief pillow mounds lie further west. The elongate fault blocks of the ridge are tilted with a westward dip and have scarps as high as 50 m. The dome was identified in the mapping data because the surface texture is rough compared to most mid-ocean ridge flows. ROV imagery shows that the roughness is caused by large, breadcrusted elongate pillows and blocky brecciated or striated lavas (Figures 11a and 11b), and sheer fault blocks topped with shattered pasty lavas that are riddled with jointed dikes and surrounded

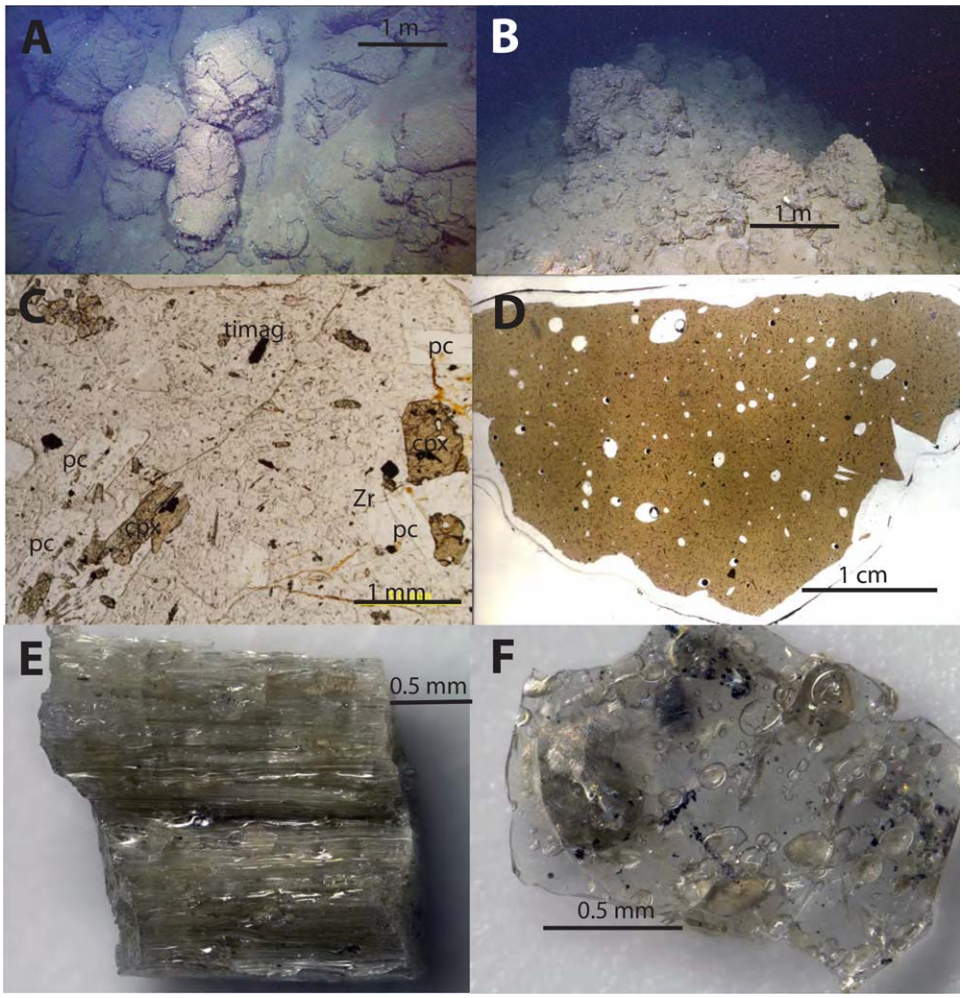

Figure 11. (a) Image of in situ pillow lavas of andesite showing similar size to that seen for basalt. (b) Image of in situ rhyolite showing blocky brecciated pasty lava. (c) Photomicrograph of rhyolite showing clear glass and assemblage of plagioclase (pc), clinopyroxene (cpx), and rare titanomagnetite (timag) and zircon (z). (d) Photomicrograph of entire thin section of dacite showing small crystal sizes, rounded vesicles, and light brown color of glass. (e) Glass fragment from rhyolite dome collected in sediment scoop from on top of dome showing clear-to-pale green glass stretched into tube pumice. (f) Fluidal fragment of rhyolitic glass also collected in sediment scoop from on top of dome with moderate vesicularity and small crystals in clear glass (Portner et al., 2014).

with abundant talus. The evolved flows have also been identified using geomorphic characteristics by an automated computer classifier (Maschmeyer et al., 2015). Many of the evolved samples are dense, but margins of fragments can be highly vesicular (Figure 11e), with elongate tube-like vesicles. Gravel samples scooped from talus slopes contained pale to light brown glassy vesicular shards (Figure 11f) that have glass stretched over enclosed crystals as described for MORB pyroclasts (Clague et al., 2009).

The faulted ridge is a few hundred meters west of the neovolcanic axis. Low-relief smooth hummocky flows of pillows resembling others on AR lie to the east. These pillow mounds are less faulted than the axial ridge and have thin sediment cover. In the northern end of AR6, about 5 km north of the large dome, ridge-parallel faults begin to bend westward to align with the PT.

PT at the north end of the AR has sediment hills surrounded by thin channelized flows (Figure 12) as seen on TT. One sediment hill is 780 by 550 m by 55 m tall (Figure 12A) and has a wide crack along its long axis. This hill is surrounded by channelized lava flows that radiate away from the hill in all directions. A second sediment hill is ~1,100 by 700 m by 90 m tall (Figure 12B). A third similar hill is only partly mapped and is located near the north central part of Figure 12. Smooth areas at the western end of the map and in the southern half of Figure 12C have low backscatter in the side-scan data (Figure 12C$_1$) and consist of thick

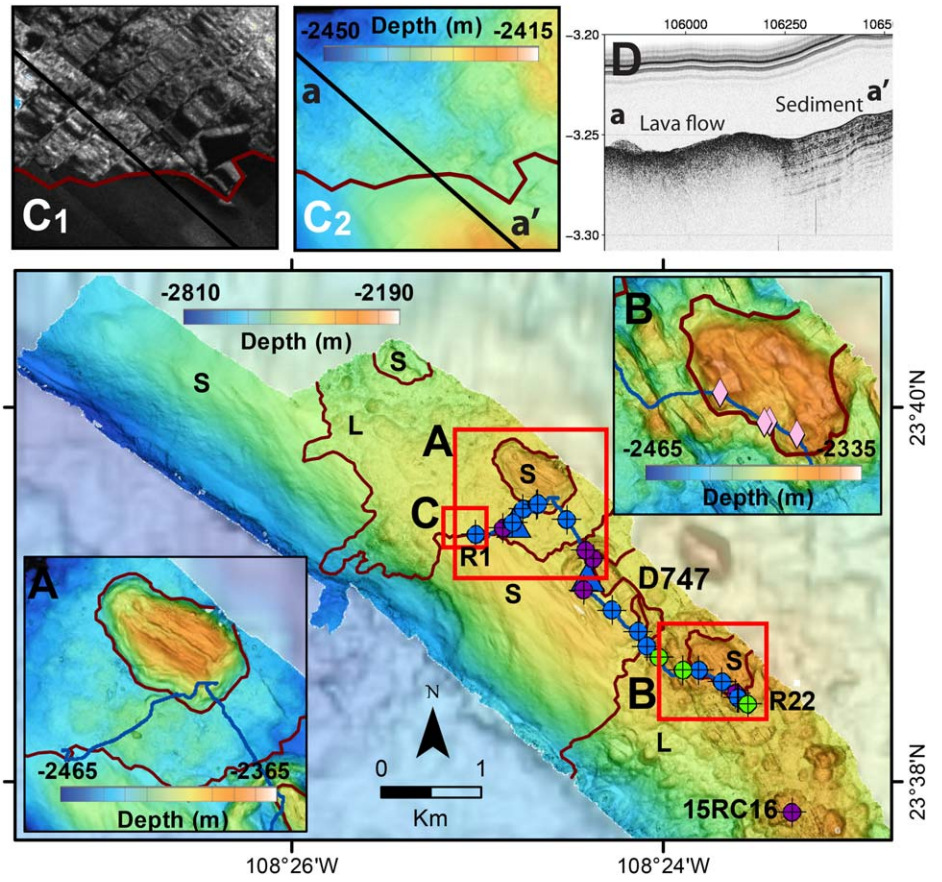

Figure 12. PT map with track of dive D747 and wax-tip core 15RC16 lava samples and radiocarbon ages of the base of cores symbolized as in Figure 3. The line separates lava-covered (L) and sediment covered (S) areas. Inset A shows an uplifted sediment hill surrounded by lava flows. Inset B shows active low-temperature hydrothermal vent sites on another uplifted sediment hill near the eastern end of the dive track. Inset C_1 includes high-backscatter (dark) lava flows north of the contact and low-backscatter thick sediment south of the contact. The bathymetric map (inset C_2) shows that the flows advanced from the NE and ramped against low sediment hills to the south and southeast. Inset D is a subbottom profile along line a–a′ in inset C_2 with sediment at least 0.05 s TWTT thick southeast of a reflective surface lava flow.

layered sediment (Figure 12D). Faults and fissures rotate from parallel to the AR at the SE end of the section to almost parallel to the PT at the central part of the mapped region. The eastern section consists of hummocky flows of pillow lava with most cut by abundant faults and fissures.

5.2. Hydrothermal Deposits and Vent Fields

5.2.1. Active Vent Fields

Multibeam surveys mapped the entire neovolcanic zone on AR and 109 separate chimneys were identified (Paduan et al., 2012, 2015). The CTD data collected by the AUV were utilized to determine if the mapped chimneys or clusters of chimneys were actively venting (Caress et al., 2015). Most chimneys were subsequently observed during ROV dives and those observations, instead of water column anomalies in the AUV CTD data, form the basis of identifying which chimneys are active and inactive. All four active vent fields are located in AR2 (Figures 5A and 5B) and occur roughly centered on the shallowest inflated portion along slightly more than 2 km of the axis. The biological communities at three of the four active vent fields (Goffredi et al., 2017) and the fluid compositions (Spelz et al., 2012), deposit descriptions, and bulk compositions (Paduan et al., 2012, 2015) are described elsewhere.

The Meyibó (Figure 5A), Pericú (Figure 5A), and Ja Sít (Figure 5B) high-temperature hydrothermal vent fields are located in or near eruptive fissures for the young channelized flow on AR2 (Paduan et al., 2012, 2015; Figure 5). The southern of these, Meyibó, has 14 active, mostly black smoker, chimneys with temperatures

as high as 359°C, and is located in a graben cutting highly fractured cones surrounded by the youngest extensive channelized flow. The northern Ja Sít field is two clusters with seven active chimneys rising above a channel in the channelized flow, ~150 m NW of the fissure. The Pericú vent field is about halfway between the first two on the northwest margin of the eruptive fissure of the same young channelized flow. It is less active than the adjacent fields, and the three active chimneys are smaller. In all these three vent fields, sulfide chimneys have formed directly on the basaltic substrate, which is partially covered with sulfide talus blocks and weathered chimney debris. The fourth active vent field, Tzab-ek (Figure 5A), located northwest of the AR2 channelized flow on an older hummocky flow, has five active black smokers up to 33 m tall with temperatures up to 355°C, two diffusely venting white smokers, and one inactive chimney. These chimneys are growing on a mound of massive sulfide approximately 5 m thick.

5.2.2. Inactive Hydrothermal Chimney Fields

Inactive chimneys are more numerous than active ones along AR and most of the 53 confirmed inactive chimneys are located on AR4 and AR5 clustered in eastern and western groups (Figures 8B and 9A) that align with slightly offset fissures (Le Saout et al., 2016). They occur along about 2.6 km of AR but starting slightly more than 10 km NNE of the northernmost active chimneys. The combined active and inactive chimneys extend nearly 20 km along the axis, centered roughly 3 km south of the large flat-topped cone in AR3. The tallest is 15 m high. The western group (along dive D394 track in Figure $8B_2$) includes chimneys that extend northward into AR5 on the western flank of the low lava shield (along dive D395 track in Figure 9A). The eastern chimneys (along dive D395 track in Figure $8B_2$) are located between the cluster of fissures NNE of the large flat-topped cones and the western line of chimneys. Some chimneys identified from the maps were not visited but are thought to be inactive, as turbid water was observed as elevated transmissometer readings on the ROV CTD and visually only near the four active vent fields. Inactive chimneys taller than ~3 m tall are readily identified in the AUV maps but as they are no longer venting, would be undetected by traditional water-column surveys.

5.2.3. Low-Temperature Hydrothermal Vent Sites on the Transform Faults

The uplifted hills of thick sediments on the transforms were found to host low-temperature vent sites. On TT (Figure 3A), venting was discovered during an ROV dive by the presence of clams and white bacterial mats on black sediment; no chimneys or vent structures were observed. A more extensive active site was found on an uplifted sediment hill on PT (Figure 12B). The site has abundant *Lamellibrachia* tubeworms among pillow lava talus, clams on black sediment between outcrops and bacterial mat surrounding cracks in nearby disrupted mudstone outcrops. A lava sample from this site has glass extensively altered to light-colored clays. No chimney structures were observed, but fluid temperatures were up to 5°C. The biological community at the PT site is described in Goffredi et al. (2017).

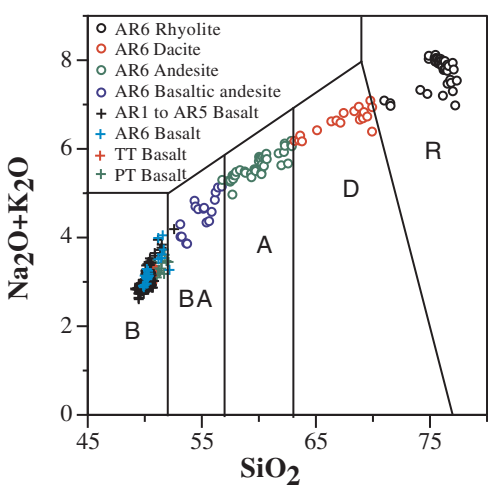

Figure 13. Alkali-silica plot with basalt from Alarcon Rise subdivided by region AR1 to AR5, and by lithology for AR6 with B, basalt; BA, basaltic andesite; A, andesite; D, dacite; R, rhyolite. Classification after Cox et al. (1979). Some hydrated rhyolite glasses have lost some Na_2O either during hydration or during analysis, resulting in slightly lower total alkalis.

5.3. Lava Compositions

Three hundred and fifty lava samples were collected on and near the ridge axis during the 2003, 2012, and 2015 ROV dives and wax-tip volcanic glass coring programs. Glasses from the AR lavas range from primitive (MgO as high as 8.87 wt %) MORB to rhyolite (MgO as low as 0.02 wt %) as a nearly continuous array of compositions (supporting information Table S1). Many of the AR MORBs are plagioclase ± olivine ± clinopyroxene phyric to ultraphyric, in contrast to the commonly aphyric MORB recovered from the EPR. Evolved lavas are abundant along AR6 (Figure 10) and are classified as basaltic andesite, andesite, dacite, and rhyolite (Figure 13; Cox et al., 1979). These classification boundaries are usually used for whole-rock compositions, and we apply them to our glass analyses.

The basalts are classified as N-MORB if $K_2O/TiO_2 < 0.10$, T-MORB if K_2O/TiO_2 is 0.10–0.20, and E-MORB if $K_2O/TiO_2 > 0.2$ (Figure 14). There is a strong correlation between MgO and K_2O/TiO_2 with N-MORBs restricted to MgO content generally >7 wt % and T-MORB generally having lower MgO contents. All basalts on AR and the transforms are N-MORB or T-MORB with the exception of one aphyric E-MORB, D746-R12, from AR3 (Figure 7). This sole E-MORB flow is located near push

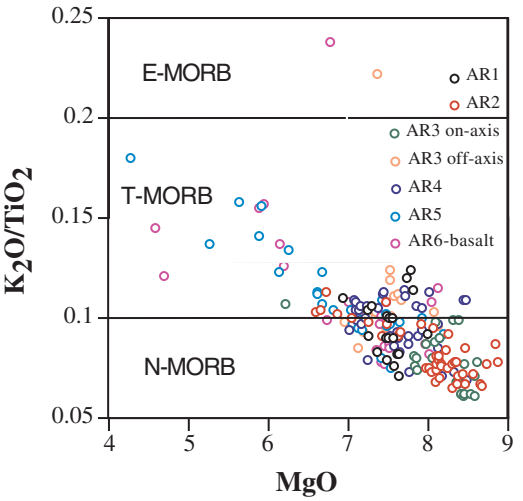

Figure 14. MgO versus K_2O/TiO_2 for AR basalts, divided by region. The overall trend of increasing K_2O/TiO_2 with decreasing MgO is steeper than the liquid line of descent for crystal fractionation (shown schematically as lines) and implies increasing admixture of enriched compositions during prolonged fractionation, as proposed for lavas elsewhere (Shorttle et al., 2016). Most of the samples classified here as "T-MORB" may be similar hybrid evolved melts. Of the two samples that plot in the E-MORB field, sample T746-R12 with higher MgO is a classic E-MORB (and the only one known from Alarcon Rise), but T740-R3 with lower MgO is an N-MORB contaminated by silicic melt/rock as discussed in the text.

cores collected in 2003 that contained E-MORB pyroclasts (Clague et al., 2009). N-MORB and T-MORB are not randomly distributed along the ridge, as lavas near the two transform faults are >70% T-MORB and lavas from AR2 and AR3 are >70% N-MORB. The most primitive (higher MgO) lavas tend to be N-MORB and more evolved lavas to be T-MORB (Figure 14). The compositions of lavas from TT and PP (Figure 15) show that they are generally evolved and slightly enriched (T-MORB).

The 10 most primitive glasses (MgO > 8.5 wt %, symbolized as red dots) on AR are exclusively N-MORB from AR2 (Figure 5) and the adjacent AR3 (Figure 7) regions. These most primitive lavas are from just three flows: the youngest extensive channelized flow, an older underlying channelized flow to the NE of the young channelized flow, and the hummocky flow that underlies the Tzab-ek hydrothermal field. Other relatively primitive glasses (MgO = 8–8.5wt %, symbolized as orange dots) are also dominantly N-MORB (46 of 52 samples), with the remainder T-MORB. These relatively primitive samples are located in AR2 and in the axial graben in AR3 to AR6, but none were found in PT, TT, or AR1.

The lavas from the TT (supporting information Table S1 and Figure 15) are mostly T-MORB with a few N-MORBs at the southeastern and northern ends of the sampled area. The glasses are fractionated with MgO = 6.7–7.6 wt % with the least primitive and most depleted (lowest K_2O/TiO_2) located near the northern end.

Lava samples from AR1 are dominantly T-MORB at the southern end and N-MORB at the northern end. Glasses contain MgO = 6.9–7.8 wt % (Figure 14). Three reanalyzed N-MORB pillow fragments from dredge D9 (Castillo et al., 2002) slightly expand the compositional range of lavas from the area.

AR2 is dominated by a chemically heterogeneous primitive N-MORB channelized flow with MgO = 8.0–8.7 wt % (supporting information Table S1 and Figure 13) with more primitive glasses near the northern end and slightly less primitive ones near the southern end. Several underlying channelized flows, also N-MORB, erupted from fissures close to those that fed the youngest channelized flow, and have similar MgO = 7.9–8.1 wt %. Dredge D8 (Castillo et al., 2002) recovered more evolved N-MORB lavas from a different flow. The cones cut by the fissures of the youngest channelized flow are T-MORB. T-MORB lavas also form a ~1 km-diameter flat-topped cone on the west side of the channelized flows (12RC1, Figure 5 and supporting information Table S1). A tall hummocky flow forms an N-MORB pillow mound complex to the west of the channelized flows in AR2. The most primitive lavas recovered from the entire Alarcon Rise with MgO = 8.85 wt % (D745-R1 and D745-R8, supporting information Table S1) occur in the southern part of this hummocky flow.

In AR3, there are no systematic changes in the compositions of lavas with distance to the axis within ~3 km of the axis (Figure 7). The lavas are a combination of T-MORB and N-MORB with most straddling the boundary (Figure 13). An E-MORB flow from the first terrace WNW of the axis has MgO = 7.4 wt % and K_2O/TiO_2 = 0.22 (D746-R12, Figures 7 and 13). Most lavas west of the axial graben have moderately evolved MgO = 7.1–7.7 wt %, whereas lavas in the graben range from MgO = 7.3–8.6 wt %, with most >7.85 wt % (Figure 7). Lava from the 600 m diameter cone has MgO = 8.3 wt % (Figure 7). The channelized flow immediately ESE of the cone is an evolved lava with MgO = 6.95–7.1 wt %; it is not as evolved as a hummocky flow with MgO = 6.2 wt % near the active axial zone.

In AR4, the flat-topped cone is constructed of N-MORB with MgO = 7.6 wt %. A channelized flow in the graben near the southern end of the section is N-MORB with MgO = 7.5–7.75 wt % (Figure 8). Hummocky and channelized flows in the northern half of the region include N-MORB and T-MORB with MgO = 7.0–8.5 wt %.

In AR5, the low shield is constructed of transitional N-to-T-MORBs (supporting information Table S1 and Figure 14) having MgO = 7.0–7.1 wt %. The northern half of AR5 is characterized by dominantly T-MORB

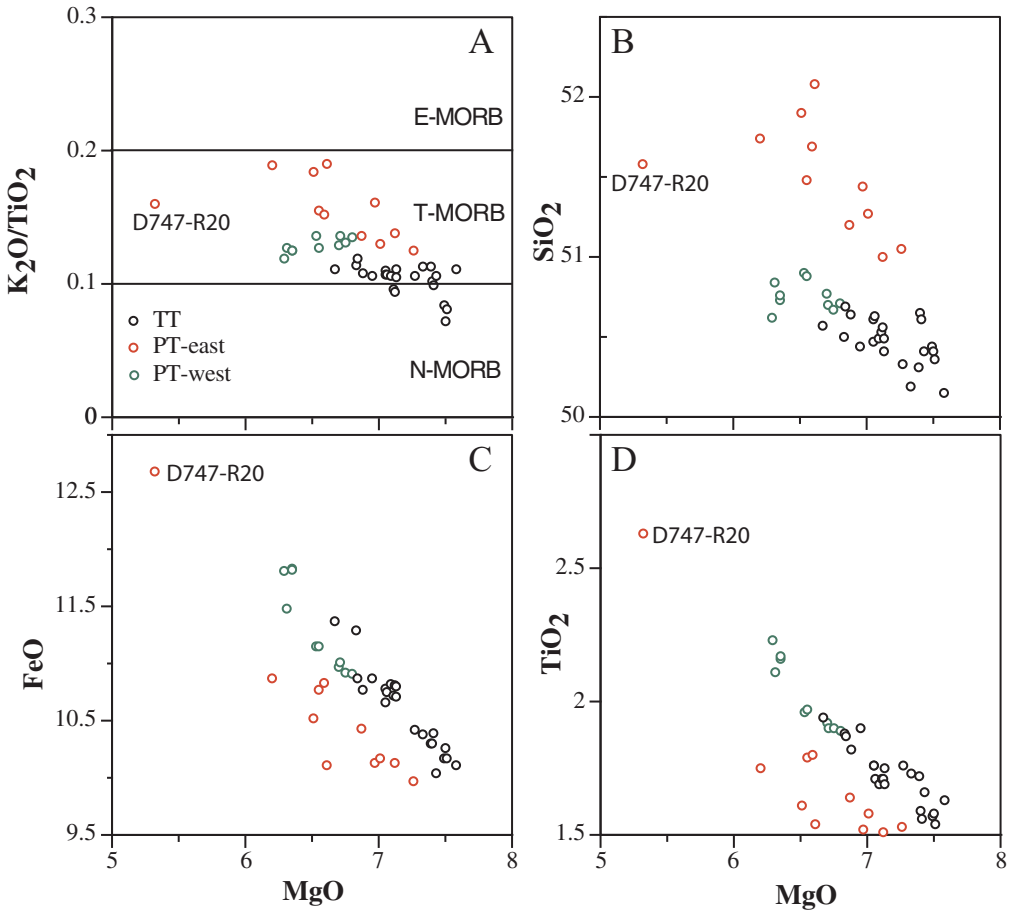

Figure 15. Chemical compositions of MORB from the TT and PT. (a) K_2O/TiO_2 versus MgO used to classify MORB types and showing that all PT and most TT MORBs are transitional (T-MORB). (b) SiO_2 versus MgO showing enrichment in SiO_2 of all but one of the lavas from the eastern PT. (c) FeO versus MgO and (d) TiO_2 versus MgO showing the depletion in FeO and TiO_2 in the same eastern group of PT lavas with elevated SiO_2. The combination of elevated SiO_2 and depleted FeO and TiO_2 is consistent with contamination of the lavas from eastern PT by rhyolitic or dacitic melt/rock. MORB sample D747-R20, discussed in the text, is labeled on each plot.

channelized flows and steep sided to low-relief hummocky flows, many constructed of highly evolved pillow lava with five sampled flows having MgO < 6.2 wt %, with the most evolved being a basaltic andesite with MgO = 4.3 wt % (this is the single basalt symbol in the basaltic andesite field in Figure 13). This sole basaltic andesite from AR5 is the only lava outside of AR6 that is more evolved than basalt. A young N-MORB channelized flow near the north end of AR5 has MgO = 8.14–8.19 wt % and is the most primitive lava in AR5.

In AR6, the southeastern low-relief hummocky flows are dominantly N-MORB with MgO = 7.3–8.0 wt % and are similar to those elsewhere. However, most of the 141 analyzed lava samples from AR6 are evolved lavas, including 41 samples of rhyolite, 21 of dacite, 41 of andesite, and 17 of basaltic andesite. The spatial distribution of the different lava types (Figure 10) shows that rhyolite occurs at four distinct sites, each with subtly different compositions. Rhyolite was collected along 3.9 km of axis including the three rough-textured structures, the largest of which is hereafter referred to as the "rhyolite dome." The most extreme rhyolite with 77.3 wt % SiO_2 (D740-R15, supporting information Table S1) contains <3 wt % FeO, ~0.6 wt % CaO, 0.15 wt % TiO_2, ~3 wt % K_2O, and 0.02 wt % P_2O_5 (Figure 16). Abundant basaltic andesite, andesite, and dacite were recovered from faults on the 10 km-long axial ridge. Together, the lavas form a near-continuum of compositions from N-MORB and T-MORB with SiO_2 = 50–51 wt % and MgO = 5.9–8.1 wt %, to rhyolite with SiO_2 = 71.0–77.3 wt % and MgO = 0.48–0.02 wt % (Figures 13 and 16). Most of the evolved lavas are plagioclase-phyric (Figures 12C and 12D), with less abundant olivine and

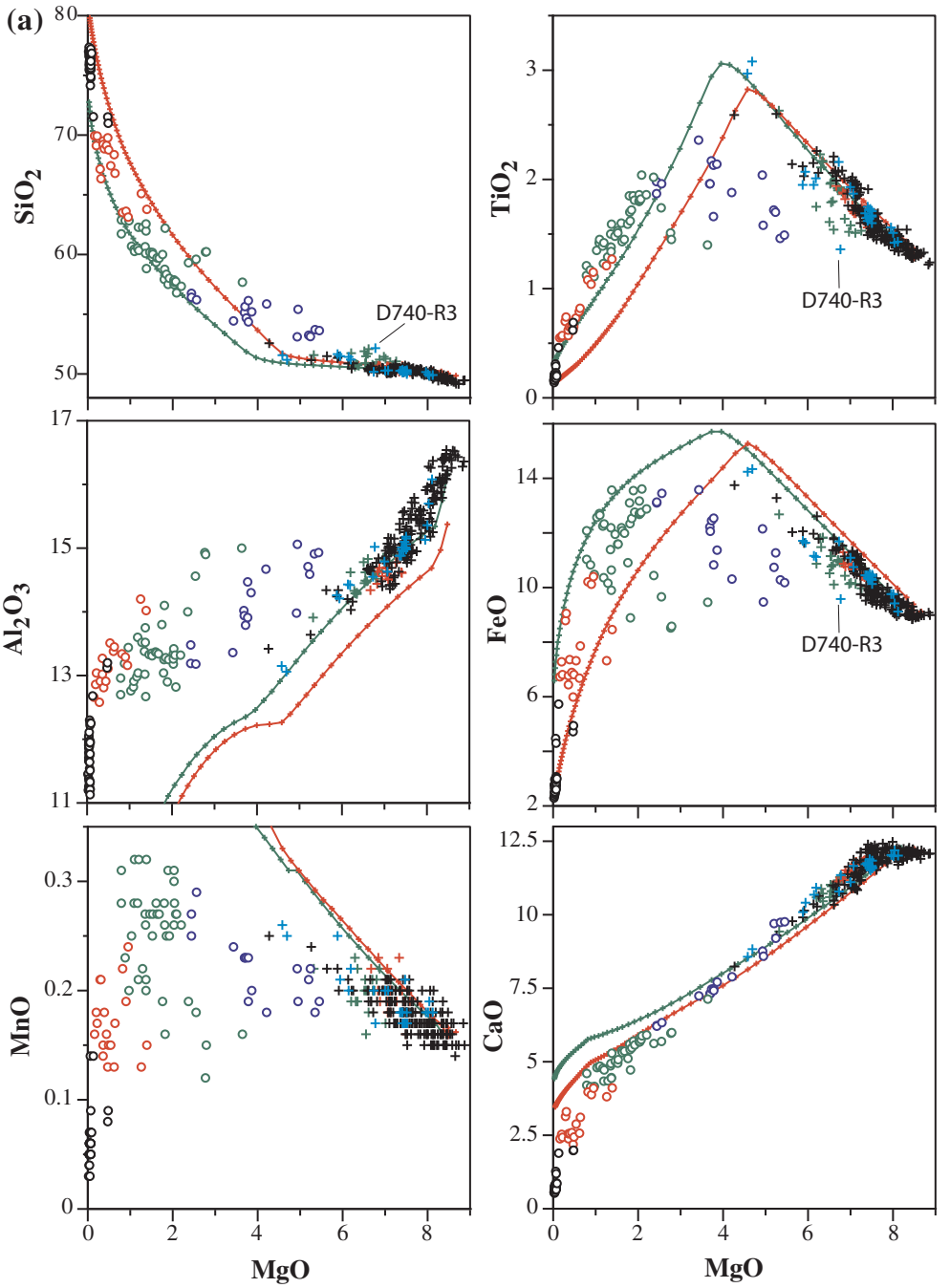

Figure 16. MgO variation diagrams of AR lavas for (a) SiO_2, TiO_2, Al_2O_3, FeO, MnO, and CaO and (b) Na_2O, K_2O, P_2O_5, S, and Cl subdivided by lithology and location. Basalt sample D740-R3 and E-MORB D746-R12 are labeled where their compositions are distinctive and discussed in the text. Most, but not all basalts, andesites, dacites, and rhyolites follow crystal fractionation trends that highlight that titanomagnetite begins to crystallize at MgO = ~4.5 wt % and apatite at MgO = ~2 wt %. Most basaltic andesites, some andesites, and basalt D740-R3 are hybrid lavas formed by mixtures of basalts with 7.5–8.0 wt % MgO and silicic lavas with MgO < ~1%. Most hybrid lavas are located north of the rhyolite dome. Two RhyoliteMELTS models are shown using sample D395-R11 (supporting information Table S1) as the starting composition with 0.20 wt % H_2O, and pressure of 0.2 or 1 kbar and oxidation state of QFM or QFM-1 for the model. See text for discussion of the models and their implications.

clinopyroxene. Mafic, and more rarely, silicic xenoliths are present in 10 rhyolite samples and in one andesite sample. Titanomagnetite, ilmenite, apatite, zircon, Fe-sulfide blebs, and rare orthopyroxene are present in some andesite, most dacite, and rhyolite.

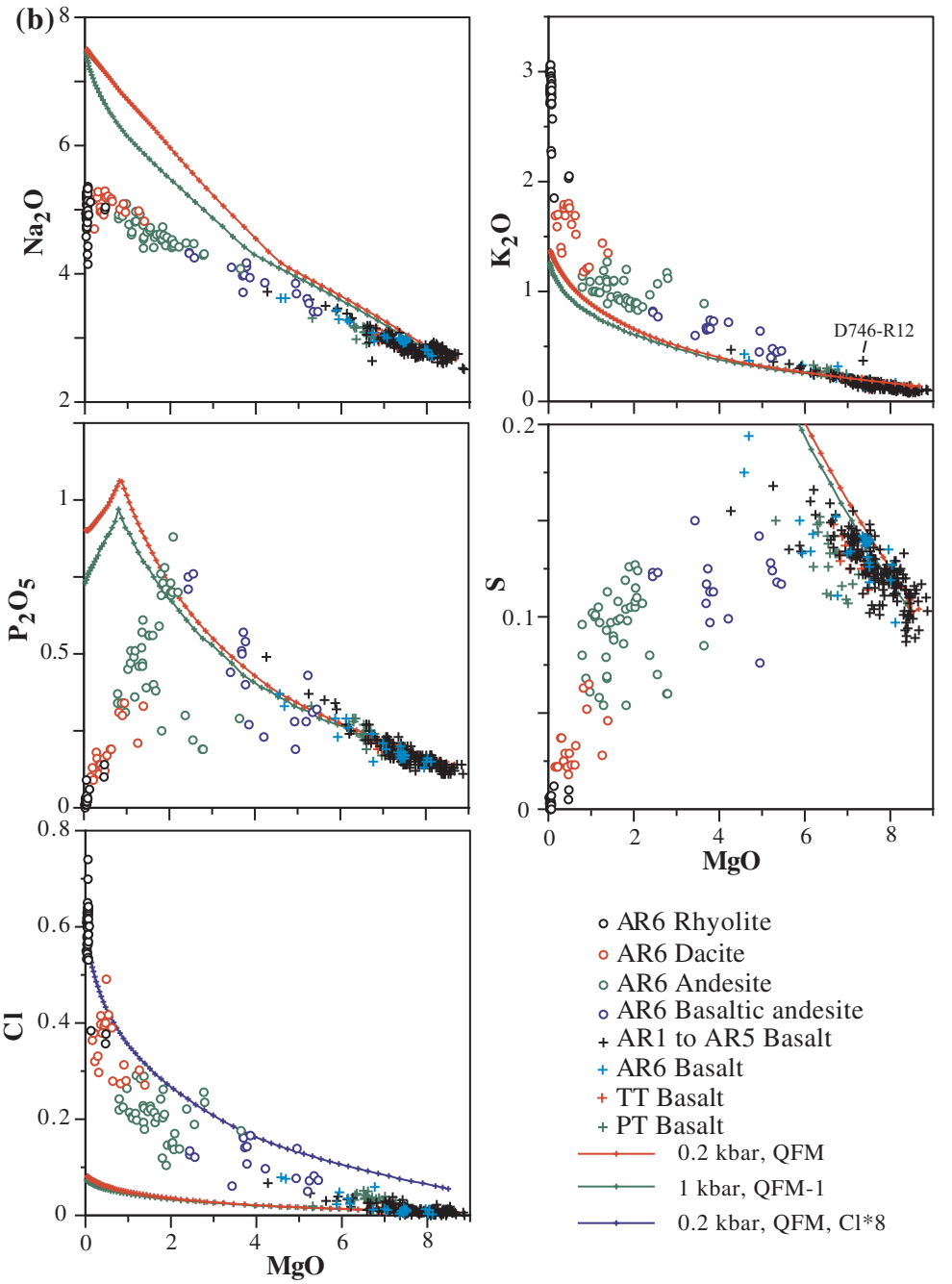

Figure 16. (continued)

The compositions of this suite of evolved lavas do not vary systematically (Figure 16); variability increases for many oxides among the dacite, andesite, and basaltic andesite compositions as MgO decreases from about 6 to 2 wt %. With decreasing MgO (Figure 16), Al_2O_3 and CaO decrease nonlinearly. SiO_2, K_2O, and Cl increase exponentially, and TiO_2, FeO, MnO, P_2O_5, and S first increase and then decrease. Na_2O increases linearly with decreasing MgO, and then decreases sharply among the rhyolites. FeO reaches a broad maxima of ~13.6 between 2 and 5 wt % MgO, TiO_2 reaches a sharp maxima of about 3 wt % at 4.7 wt % MgO, and P_2O_5 reaches a sharp maximum of ~0.85 wt % at ~2 wt % MgO. Dredge sample ALAR0D4-1 (Castillo et al., 2002) and 15RC6 (supporting information Table S1) have the highest FeO and TiO_2, the lowest Al_2O_3, and

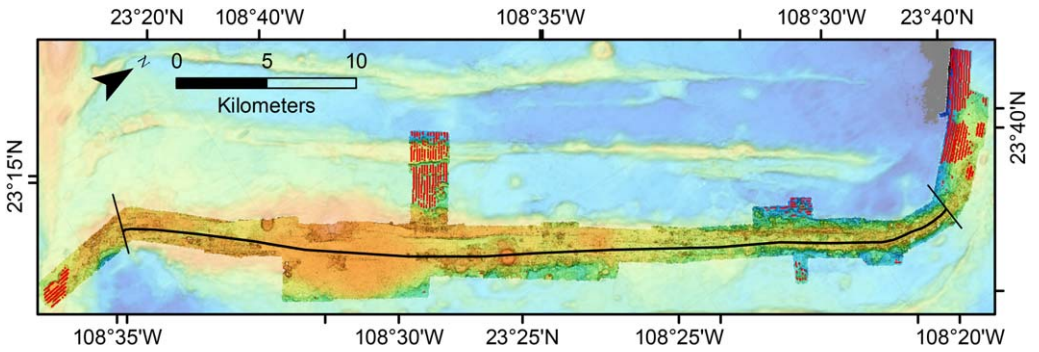

Figure 17. Map showing distribution of sediment detected by the chirp subbottom sonar on the AUV. The red symbols show the portions of the profiles where sediment was detected, indicating thickness >~3 m. The sediment thickness reaches a maximum on TT and PT where full chirp penetration is achieved, indicating sediment >50 m thick, and at the northwest end of the cross-ridge survey AR3 where sediment reaches a maximum thickness of ~35 m.

close to the lowest CaO of all lavas from AR; they are likely from the same flow and represent the magma composition when titanomagnetite first started to crystallize.

The few lava samples collected west of the axial ridge in AR6 include an evolved T-MORB, a basaltic andesite, and an unusual basalt sample, D740-R3 (Figure 10A), that has slightly high K_2O and SiO_2, and low P_2O_5, TiO_2, and FeO (supporting information Table S1). The combination of high K_2O and low TiO_2 results in high K_2O/TiO_2, similar to ratios in E-MORB (such as sample D746-R12 from AR3 Figure 7), but D740-R3 is not an E-MORB; its origin is discussed in section 6.2.2. The southeastern low-relief hummocky flows are less faulted and have thin sediment cover compared to the axial ridge or flows west of the axial ridge. They are dominantly N-MORB with MgO = 7.3–8.0 wt %.

The flows on PT have Na_2O-rich (~3–3.2 wt %) T-MORB compositions (supporting information Table S1 and Figure 15a) having MgO = 5.32–7.26 wt %, with 17 of 21 samples between MgO = 6 and 7 wt % (Figure 15). The samples from PT fall into two groups, a western group that are similar to the basalts from the TT and an eastern group closer to AR6 that have high SiO_2 (Figure 15b) and low FeO (Figure 15c) and TiO_2 (Figure 15d). An outlier is D747-R20, which instead has characteristics similar to sample D740-R3, but less extreme.

5.4. Sediment Distribution Determined From AUV Chirp Subbottom Data

The subbottom chirp system on the AUV provides information on sediment thickness below the AUV track lines. Most of the AR has sediment cover too thin to detect, and ROV observations and push core penetration suggest that seismically undetected sediment is <~2–3 m thick. Subbottom profiles show distal areas to the east of AR4 and AR5 have thin, but easily detected sediment cover (Figure 17). On the transforms, in areas not covered by lava flows, sediment was >50–70 m thick and sometimes clearly layered (Figures 12D and 17), but in other places was disrupted, steeply dipping, or structureless. The uplifted sediment hills were observed from ROV to be disrupted mudstones, but where basement was not imaged, or sediments were partially lithified or disrupted to the point of being structureless, the difference between lava and sediment was more ambiguous in the profiles. As expected, surface roughness is masked away from the neovolcanic axis (Figure 7) as sediment thickness increases in cross-axis region AR3 (Figure 18) from undetected within the axial graben and on the first outward sloping ridge (where observations and measurements from the ROV suggest sediment is ~0.3 m thick), to <3 m in the valley 4.5–2.5 km west of the axis, to ~10 m on the next lower ridge about 5 km west of the axis, to 15 m on the crest of the ridge about 5.5 km west of the axis, to 35 m in the most distal valley about 6.5 km west of the axis.

5.5. Sediment Cores and Inferred Ages of Underlying Lava Flows

5.5.1. Ages on AR

Even in the axial and proximal regions of AR, many lava flows are partly covered by enough sediment to sample using 30 cm or 1.2 m long push cores deployed from the ROV (supporting information S1). Sediment on AR is mainly tuffaceous mud (Portner et al., 2015) with most samples containing volcanic glass shards, broken plagioclase crystals, planktic and benthic foraminifera, diatoms, radiolarians, sponge spicules,

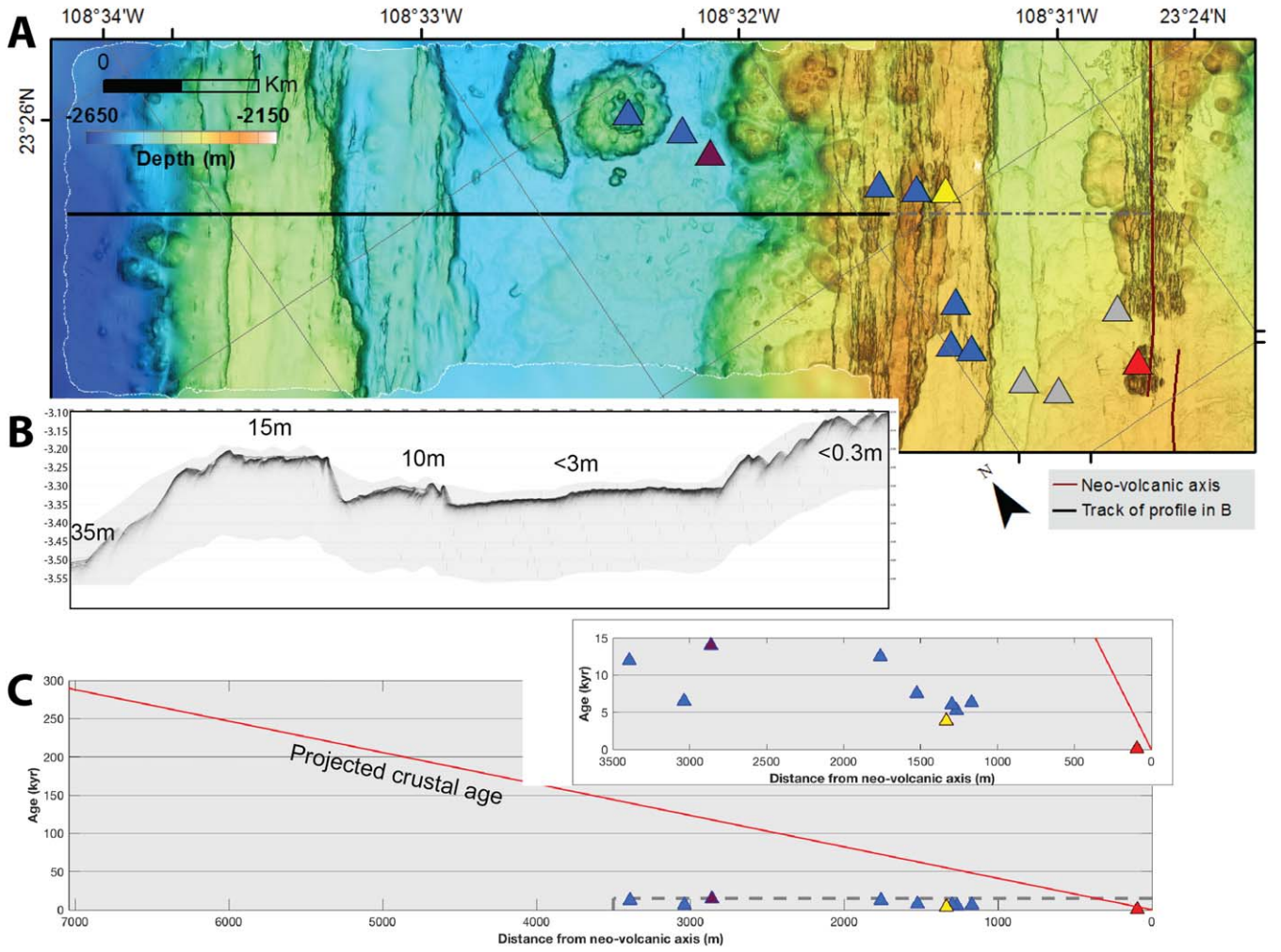

Figure 18. (a) Map of AR3 showing locations of dated cores, symbolized as in Figure 3. Black line indicates the location of illustrated subbottom profile (Figure 18b). (b) Subbottom profile shows up to 35 m of sediment at the distal NW end of the line and decreasing thickness of sediment approaching the ridge axis. The area with <3 m of inferred sediment cover is based on ROV observations, and the area with <0.3 m of inferred sediment cover is based on maximum lengths of collected push cores. (c) The ages of base of cores (symbolized as in Figure 3) are plotted as a function of distance from the axis, with a projected crustal age-distance line in red, based on a half-spreading rate of 2.43 cm/yr (DeMets et al., 2010). (c inset) Expanded scale of ages shows that cores outside the axis are nearly an order of magnitude younger than projected crustal ages and demonstrate repaving of areas as much as 3.5 km from the spreading axis by much younger flows.

and fecal pellets. Foraminifera and other carbon-bearing fossils were sieved from the bottom interval of the cores and ^{14}C age dated (supporting information S1) to yield an estimate of the minimum age of the underlying lava flows upon which they were deposited.

Ages of basal sediment in cores from AR (supporting information Table S2 and supporting information Figure S1) range from modern (27 cores or nearly 25% of the cores dated) to 14 ka. Eleven cores had basal ages between 9 and 18 ka, 18 were between 3 and 9 ka, 19 were between 1 and 3 ka, 23 were between 400 years and 1 ka, and the remaining 21 were <400 years. Most of the modern and <1,000 year dates came from cores <15 cm long (supporting information Figure S1). One modern age, however, was determined on foraminifera from 43 cm depth in the core, suggesting that bioturbation added modern foraminifera deep in some cores. Ten of the ages >5 ka are from samples collected off axis in the cross section away from the axis (Figure 7) and have broadly increasing age with increasing distance from the axis (Figure 18). Five cores with two or three dated horizons yielded increasing ages with depth (supporting information Figure S1) consistent with average sediment accumulation rates between ~4.3 and 28 cm/ka with all but one

near the low end of the range. However, core D396-PC77L yielded modern and older-over-younger ages midcore; again, this is most probably due to bioturbation.

The oldest dated flows from AR1 (Figure 4) are 3.8, 2.9, and 2.1 ka; five more yield ages $<$1 ka, and seven samples yielded modern ages. All 15 cores contained adequate foraminifera to date. Modern ages at the base of 8–29 cm cores were especially common from this portion of the ridge axis with 6 of the 27 such samples from AR. These modern ages at depth in the cores indicate extensive bioturbation or other sediment redistribution processes.

Most flows in AR2 (Figure 5) generally had too little sediment to retain in the core tube and only eight cores were recovered during four ROV dives. A hummocky flow dissected by the fissures that fed the young channelized flow yielded an age of 295 years. The Tzab-ek active vent field is located on a 1.4 ka hummocky flow.

On AR3 (Figure 7), minimum radiocarbon ages for lava flows generally increase away from the axis, but ages for flows in the valley west of the axis (Figure 18) are more than a factor of ten younger than the $\sim$120–140 ka basement age calculated using a half-spreading rate of 2.43 cm/yr (DeMets et al., 2010). Our most distal core, in the crater of the 600 m-diameter cone about 3.6 km west of the axis, yielded a basal age of 12.0 ka at 115–116 cm depth compared to the predicted crustal age of 140 ka. A 13.7 ka channelized flow $\sim$2.8 km from the axis is the oldest dated flow from the cross section. At $\sim$1.7 km and $\sim$1.5 km from the axis, ages of 12.0 and 7.5 ka were determined. At 1.2–1.3 km from the axis, four flows yielded ages of 3.9, 5.3, 6.0, and 6.3 ka. In the graben immediately west and within 1 km of the axis, four cores yielded modern ages or lacked adequate foraminifera to date.

Cores from AR4 (Figure 8) range from 268 years to 2.2 ka, and three of the shorter cores yielding modern ages. The oldest $>$1 ka-old flows were from a small pillow cone near the west margin of the axial graben, and from two small channelized flows near the deepest part of the axis in this region. The inactive hydrothermal chimneys near the northern end of AR4 are on or near flows dated at 268 years to 1.0 ka.

The shield in AR5 is dated by three cores (Figure 9) with statistically overlapping ages suggesting a $\sim$320 $\pm$ 30 years minimum age. This age is more recent than estimated from the spreading rate and extension indicated by the faults and fissures that cut the shield (Le Saout et al., 2016). Northward, 16 mostly hummocky flows were dated and range from 89 years to 1.3 ka, with two flows yielding modern ages.

A major focus on AR6 (Figure 10) was to determine the timing of emplacement of the rhyolite, dacite, and andesite and 53 cores were collected to accomplish that goal. Nine of these were long cores, with the longest recovering 102 cm of sediment. The blocky surface of the dome made core sampling extremely challenging; often sediment was observed between blocks beyond the reach of the manipulator. Occasionally, basal sediment fell out of the core tube before it could be secured on the ROV. In addition, 21 cores yielded too few foraminifera to date. Exponential decay of ^{14}C and bioturbation makes it difficult for ^{14}C ages to be too old but very easy for them to be too young. The three oldest long cores provide minimum ages for one andesite flow and two dacite flows from 11.0 to 11.7 ka, and four of the long cores were dated at two depths in the core and ages are in expected young-over-old sequence (supporting information Figure S1). Basal sediments in cores on multiple dacite and andesite flows span from 11.3 to 3.4 ka and from 11.7 to 1.1 ka, respectively. The ages of the three chemically distinct smaller rhyolite flows are unconstrained. Ten cores were collected on the rhyolite dome and all but one yielded ages from 686 years to modern with the one exception being 4.4 ka, establishing that the rhyolite dome is at least this old.

To better constrain the age of the rhyolite dome, the sedimentology of the 11.7 and 11.3 ka-old cores from the west flank of the dome were examined and colorless rhyolite and pale brown dacite glass were identified throughout the cores, including in the basal dated cm, thereby confirming a minimum age of some dacite of 11.7 ka and establishing that as a minimum age of nearby rhyolite. This suggests a minimum age of the rhyolite dome is 2.7 times older than the oldest age determined for sediment on top of the dome, thus illustrating the difficulty of sampling the oldest sediment on the blocky rhyolite dome.

Short cores ($<$12 cm long) collected on the hummocky N-MORB flows along the SE edge of the axial horst on AR6 yield ages of modern to 280 years, a core on another T-MORB flow closer to the dome yielded an age of 568 years, and those on the neovolcanic axis had too little sediment to core. Therefore the MORB pillow mounds in AR6 postdate eruption of all evolved lava compositions based on sediment cover and determined minimum ages.

5.5.2. Ages on TT and PT

Ages from the TT (Figure 3) are as old as 17.9 ka but are far fewer in number as most recovered sediment contained no foraminifera or too few to date. One long core that sampled to the underlying channelized lava flow yielded stratigraphically consistent ages of 6.7 ka at 40 cm depth and 7.8 ka at 75 cm depth in the core, so the underlying flow erupted a minimum of 7.8 ka ago. The uplifted hills consist of fine micaceous silty sands with consistent ages of 17.9 and 17.7 ka at the maximum penetration of the cores. These two cores did not reach underlying lava flows, but to firm sediment that the cores could not penetrate. Seven 17–25 cm-long cores and a 48.5 cm-long core had inadequate foraminifera to date the basal sediment. Minimum ages for undisrupted hummocky flows are 3.0 and 2.1 ka. Nearby

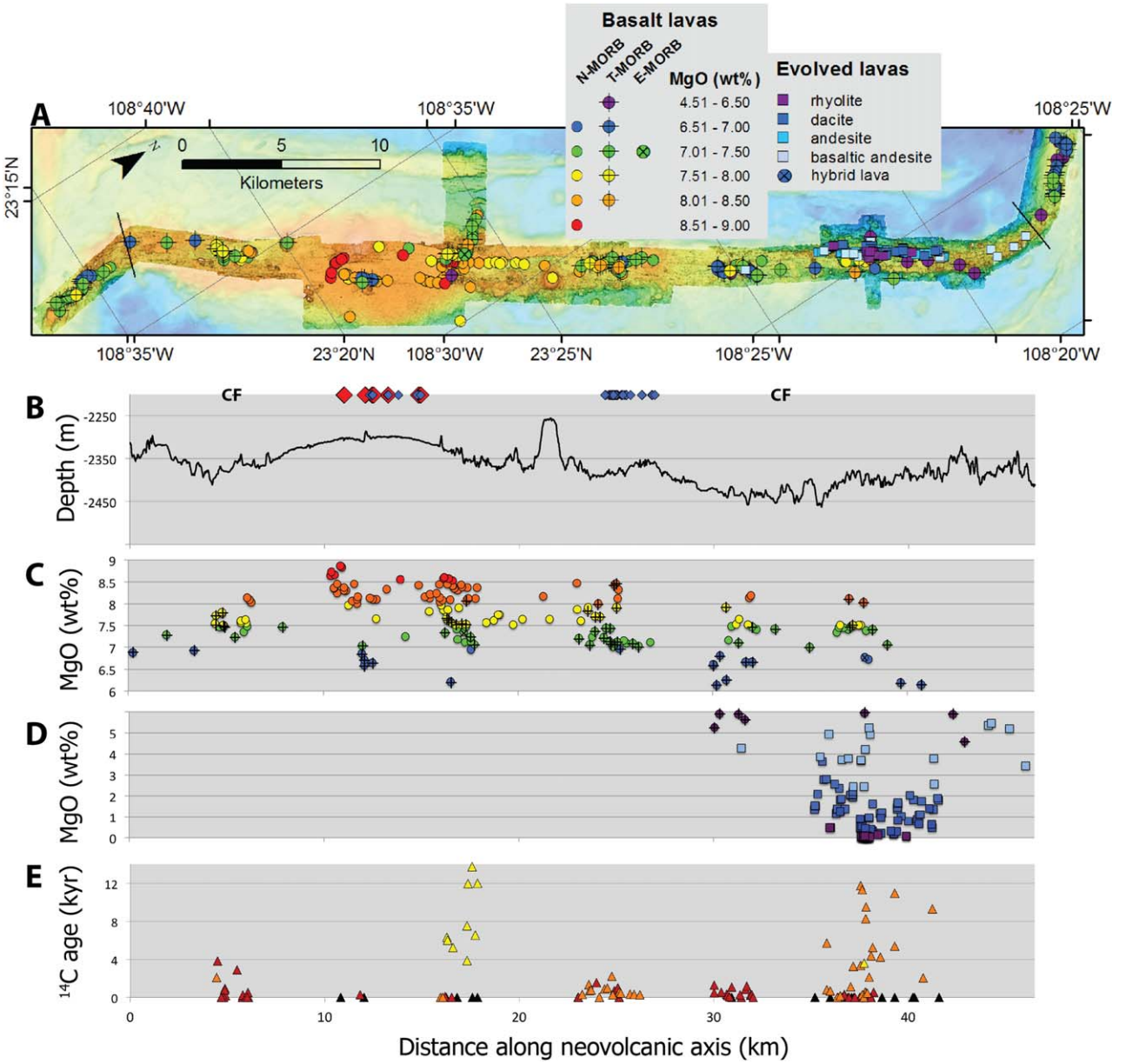

Figure 19. (a) Plot along axis showing AUV map and lava samples, color coded by lithology for evolved lavas and MgO content for MORBs. T-MORBs and N-MORBs shown with separate symbols. (b) The profile of axial depth along strike with CF indicating the northern and southernmost channelized flows and red and blue diamonds, respectively, showing the locations of active and inactive hydrothermal chimneys (along top of figure). (c) MgO of MORB lavas with T-MORBs and N-MORBs with separate symbols for lavas with MgO > 6 wt % and (d) MgO of evolved lavas with MgO < 6 wt %, symbolized by lithology as in Figure 10. (e) The distribution of radiocarbon ages (triangles) projected along the axis with those within 0–500 m of the axis in red, between 500 and 1,100 m in orange, between 1,100 and 3,400 m off-axis in yellow, and cores with no foraminifera in black.

hummocky flows have abundant faults and fissures and are buried beneath thicker sediment, so are inferred to be older.

Sediment thickness on top of the flows is variable and suggests a wide range in ages. Radiocarbon ages were obtained from only two of nine cores as the others lacked adequate foraminifera to date. A 25 cm core on the western channelized flow yielded a minimum age of ~4.8 ka. The eastern dated site is located in a depression within a partial ring-shaped hill; it yielded a minimum age of 2.9 ka at ~110 cm depth and a second age halfway up the core of 1.4 ka. The sediment at this site accumulated at ~38 cm/ka compared to ~5 cm/ka at the nearby site on the channelized flow. Cores collected off the lava flows on PT consist of firm sediment, and sampled the top of the >70 m-thick sediment (0.07 s TWTT), determined by the AUV chirp subbottom system.

6. Discussion

6.1. Distribution of Characteristics Along Axis

Many morphologic, geophysical, and geochemical parameters have been postulated to vary along segments (summarized in Macdonald, 1998). Nearly all these studies have examined the fast spreading EPR, although Kappel and Ryan (1986) and Perfit and Chadwick (1998) specifically addressed intermediate-rate ridges. Here, we extend the morphologic and geochemical analysis to the intermediate-spreading AR (Figure 19).

6.1.1. Axial Depth

Macdonald et al. (1984), Lonsdale (1989), Carbotte and Macdonald (1994), and Toomey and Hooft (2008), among others, proposed that the shallowest portion of the neovolcanic zone in ridge segments is centrally located and marks the locus of mantle upwelling and melt delivery for the segment. The depth of the center of the neovolcanic zone is shown in Figure 19b. The shallowest feature along the segment is the large flat-topped cone in AR3, which is located ~22 km from the TT and ~25 km from PT, so located close to the middle. On the other hand, the broad inflated portion of the segment largely paved by the extensive channelized flow, which we have shown is the youngest feature on the AR, is about 11 km north of TT and 36 km south of PT. Using this measure of the shallowest portion of the ridge, the most magmatically robust portion of AR is not centrally located. Likewise, the deepest part is just south of the rhyolite dome and not at the distal ends of the segment.

6.1.2. Width of Fissures

Macdonald (1998) suggested that fissure width varies along a segment of ridge with the widest fissures concentrated near the shallowest inflated central portion of the segment. The fissure system that fed the extensive channelized flow is nearly 100 m wide (Figures 5A, 5B, and 6A) whereas farther northeast and southwest, fissures are no more than a few meters wide. This wide fissure almost surely is a measure of extension during repeated eruptions along the same fissure system, as observed during the 2011 eruption on Axial Seamount (Caress et al., 2012; Clague et al., 2017) that reused and widened fissures also active in 1998 (Chadwick et al., 2013). This characteristic to reuse the same fissures and widen them may simply require that the dike feeding the eruptions in the shallowest portion of the axis can migrate downslope along axis to leave the eruptive fissure drained. Downslope, the eruptive fissures would be largely sealed at the end of eruptions by hummocky flows, which appears to be the case at AR.

6.1.3. Distribution of Channelized and Hummocky Basalt Flows

The relationship between magma viscosities and volcanic landforms, based on analysis of Alarcon Rise lavas and mapped flow types is presented in Martin et al. (2012). By far the largest single flow on the AR, the channelized flow that dominates AR2, covers at least 15.95 km^2 (Figures 5 and 6). For comparison, the 2005 9°N EPR flow is 14.6 km^2 (Soule et al., 2007) and the 1998, 2011, and 2015 flows on Axial Seamount are 7.1–11.5 km^2 (Clague et al., 2017). The 1986 North Cleft flow covered 2.8 km^2 and other historical flows cover <1 km^2 (summary in Clague & Paduan, 2009).

Channelized flows occur only in AR2 north of 23°19′N, AR3 (both on and off axis), AR4, and AR5 south of 23°31′N. Such flows, interpreted to represent high effusion rate flows (Griffiths & Fink, 1992; Gregg & Fink, 1995) occur along ~27 km of the axis (Figure 19b). Such flows do not occur within about 5 km of TT or ~15 km of PT. In a broad way, the distribution of flow types indicates that eruptions nearer the segment center are more vigorous than those farther away. White et al. (2000, 2002) showed a similar decrease in inferred effusion rates toward the ends of third-order (overlapping) segments (using nomenclature of Macdonald et al., 1991) that we observed here for a first order segment bounded by transform faults.

6.1.4. Distribution of Hydrothermal Vents and Chimneys

Haymon et al. (1991) and Macdonald (1998) proposed that active hydrothermal vents were concentrated near the inflated central portion of the segment axis. Four active hydrothermal vent fields are located on AR2, the shallowest region of the segment. Just as the shallowest region is not in the center, the active vent fields are located between 11 and 15 km of the TT, but 32–36 km from the PT (Figure 19b). Three of four active fields are located on or near the fissure that fed the youngest channelized flow on AR. The fourth is located just a km away from the recent eruptive fissure. Inactive hydrothermal chimneys occur along ~4 km of the ridge axis ~11 km ENE of the shallowest zone and close to the center of the axis. The active vents are indeed located on the most inflated section of the axis, but not centrally located. In the recent past, active vents were located closer to the center point along the axis, but the currently active vent fields are all near the crest of the inflated section of the axis, further to the south.

6.1.5. Distribution of Lava Flow Ages

Another proposal is that the shallowest inflated section of the segment has the youngest lava flows (e.g., Macdonald, 1998). AR2 is clearly the youngest region on AR, although that view is biased by the area covered by the extensive young sheet flow. We collected cores on other flows and dated their bases in part to test this premise. The results of all our age data are plotted as a function of distance along the axis in Figure 19e, although it does not show flows where there was inadequate sediment to collect. The cores that had inadequate foraminifera or yielded modern ages still inform the discussion, as they had adequate sediment to recover so are significantly older than flows with too little sediment to core.

The extensive channelized flow has so little sediment that no cores could be collected, despite considerable effort spent trying to locate a suitable location. The hummocky flows split by the eruptive fissure that fed the extensive channelized flow yielded a core that was dated at 295 years. The age of the oldest flow on AR2 is the off-axis flow that is both the substrate for the Tzab-ek vent field and the most MgO-rich lava on AR is 1.4 ka. The axial graben is younger than this flow, which is offset by the SW graben-bounding fault. Eighteen cores were dated from the axis of AR1, of which half yielded modern ages. Other cores yielded ages from 169 years to 3.8 ka with 7 older than 500 years. AR4 has 11 axial flows dated at >500 years, AR5 has 5 such flows, and AR6 has 24. AR6 had 17 flows older than 2 ka, and by far the oldest ages on AR. Therefore, the proposal that the shallowest portion of the ridge has the youngest flows is supported at AR. Older ages are also, not surprisingly, found farther off axis.

6.1.6. Distribution of MgO Content of Basalt Glasses

Numerous studies of individual or multiple ridge segments (e.g., Langmuir et al., 1986) have shown that the most MgO-rich melts erupt near the shallowest portion of the segment. MgO content of glasses is highest near the shallowest portion of the neovolcanic zone (Figures 19b and 19c), although lavas with >8 wt % MgO are found along ~32 km of the axis of the neovolcanic zone from 6 km northeast of TT to 8.5 km southwest of PT. Lavas with >8.5 wt % MgO occur from 10 to 25 km from TT and 23 to 36 km from PT. The maximum MgO content is just 10.5 km north of TT. The proposal that the shallowest central inflated zone coincides with the hottest, most MgO-rich lavas (e.g., Macdonald, 1998 and many prior and subsequent studies) is broadly confirmed on AR. The AR data also seem to support the concept of a somewhat less centralized zone of upwelling and melt delivery along the segment and crustal emplacement of dikes away from that shallowest ridge portion. Those laterally emplaced dikes cool with concomitant MgO contents decrease as they propagate away from the hottest central zone.

The compositional variability of the extensive young channelized N-MORB flow in AR2 (Figure 5), with MgO = 8.01–8.73 wt % (supporting information Table S1), is similar to that observed elsewhere for large flows with multiple analyzed samples (Goss et al., 2010; Rubin et al., 2001).

6.2. Location and Formation of Evolved Lavas

6.2.1. Distribution of Evolved Lavas

Rhyolites from AR6, with up to 77.35 wt % SiO_2 (Figures 10 and 19 and supporting information Table S1) are the first rhyolites recovered from the submarine mid-ocean ridge system. The occurrence of basaltic andesite, andesite, dacite, and rhyodacite near the ends of ridge segments has long been recognized (e.g., Byerly et al., 1976; Christie & Sinton, 1981; Clague et al., 1981; Perfit & Fornari, 1983; Regelous et al., 1999; Sinton et al., 1983) and various models proposed to explain their occurrence at these locations due to magma cooling against older crust. Only a few of these sites are near ridge-transform intersections (Regelous et al., 1999; Schmitt et al., 2011; Sinton et al., 1983, Stakes et al., 2006). More recent detailed studies, mainly of

basaltic andesite, andesite and dacite near the 9°N overlapping spreading center (Wanless et al., 2010, 2011, 2012) relate the occurrence to proximity to a large-scale (~27 km of limb overlap, and ~6–8 km of segment separation) overlapping spreading center. The most evolved lavas are located along ~4 km of the propagating eastern limb, but 16 km from the rift tip. Basaltic andesite occurs within ~9 km of the propagating western rift tip. Other rare basaltic andesite, andesite and rare dacite flows occur along nearly 300 km of the Pacific-Antarctic Rise (e.g., Freund et al., 2013), but these evolved lavas are associated with the intersection of the spreading ridge and the Foundation Seamount chain rather than to ridge segmentation.

Evolved lavas of basaltic andesite, andesite, dacite, and rhyolite (Dreyer et al., 2012) are located along the length of AR6 (Figure 19d), occurring along approximately 6, 6.5, 5, and 4 km of the axis, respectively. Therefore the northernmost basaltic andesite, andesite, dacite, and rhyolite are located approximately 4.5, 5, 6.5, and 6 km SSW of PT. The evolved lavas at AR occur much closer to the segment end than at 9°N. Notably, the cool boundary at AR is continental crust north of the PT compared with still young ocean crust at the 9°N overlapping spreading center, so the evolved lavas on AR may form closer to a cooler boundary than at 9°N. The relative coolness of the bounding continental crust north of PT may result in the formation of rhyolite, unknown elsewhere along the submarine mid-ocean ridge system. A major difference between AR and the other sites is that at AR eruptions have apparently reverted to MORB compositions in the last ~1.1 ka, presumably as magma supply has increased.

6.2.2. Magma Evolution

Early models of the formation of evolved basalts on mid-ocean ridges proposed simple crystal fractionation of an assemblage of mineral phases dominated by plagioclase and augite with lesser olivine (e.g., Clague & Bunch, 1976). With continuing cooling and crystallization further decreasing MgO content of the melt, the compositions of the fractionating phases change and titanomagnetite and pigeonite are required as additional fractionating phases to produce andesite and rhyodacite on the Galapagos Rift (see Clague et al., 1981, Figure 5; Perfit & Fornari, 1983). Recent detailed modeling incorporates concurrent assimilation and fractionation to account for elevated Cl and K_2O (and other incompatible elements) contents and low oxygen isotopic ratios of andesite and dacite from the Pacific-Antarctic Rise (Freund et al., 2013). More complex modeling of observed trace and incompatible element behavior patterns indicates partial melting of amphibolite-greenshist grade ocean crust, coupled with fractional crystallization and assimilation (Wanless et al., 2010, 2012) to produce andesite and dacite on mid-ocean ridges. The complexity of these models arose because simple fractionation models, such as can be modeled by MELTS programs (Ghiorso & Sack, 1995; Gualda et al., 2012; Smith & Asimow, 2005), did not produce compelling matches to the data under likely conditions.

The AR evolved lavas represent a complete sequence of lavas from MORB to rhyolite (Figure 10). As found by Wanless et al. (2010, 2012) for the northern EPR andesites and dacites, simple crystal fractionation did not reproduce the variations among the Alarcon basalts to rhyolites (Figure 16). Trace element, radiogenic, and stable isotopic compositions of zircon in the Alarcon rhyolite precludes more than a minor role for continental crust in the formation of the silicic lavas (Portner et al., 2015). Two crystal fraction liquid line of decent models using RhyoliteMELTS (Gualda et al., 2012) are illustrated in Figure 16 using the same starting parent composition (sample D395-R11 in supporting information Table S1). A number of oxides or elements could not be matched, especially Al_2O_3 and Cl (Figure 16). The peak in FeO_T and TiO_2 marks the onset of titanomagnetite crystallization and is best matched using FMQ-1. At higher pressures, SiO_2 does not increase as high as observed in the samples (Figure 16), suggesting P is less than 1 kbar. Superposed on this magmatic evolution is assimilation of a seawater-derived component that elevates Cl far above concentrations expected by fractionation alone (Wanless et al., 2010; see their Figure 6). A range of liquid lines of descent from different basaltic starting compositions, but similar to the our starting composition, also yield Cl concentrations in dacite and rhyolite of $<$0.1% (Figure 16; Wanless et al., 2010), in contrast to the observed ~0.4% for dacites and 0.6% for rhyolites on AR6. In the rhyolites, Cl is elevated by a factor of ~8 times the model concentrations, suggesting Cl assimilation most likely started early in the fractionation process in order to match the highest Cl in basaltic andesites. Like Cl, K is also overenriched in the rhyolites, although to a smaller degree, yet similarly highly incompatible P_2O_5 is not. P_2O_5 reaches a peak indicating the onset of apatite crystallization, but the peak is at lower MgO than the models suggest. This misfit might be caused by Cl in the melts being far higher than in the models, with higher Cl in melt increasing the stability field for apatite. Perhaps the largest model misfits are for Al_2O_3 and CaO, which decrease too rapidly

in the models, and Na_2O, which increases too rapidly in the model. The implication is that plagioclase in the model is too calcic. A decrease in the initial water content can shift the plagioclase composition to less anorthitic, but reasonable variation in starting H_2O-contents are not expected to alter these findings. A broader range of liquid line of descent models will be explored in a future paper focused on the mineral chemistry of the sample suite. As simple crystal fractionation from a single parental magma cannot reproduce the Alarcon basalt to rhyolite variations and given that mixing and/or hybridization of magmas is evident along the AR (see below), a more complex model that will be explored is that the dacite and rhyolite lavas are produced through fractionation in a continuously recharged crystal mush.

We divide the apparent continuum of compositions into three parts. The first part is a series of basalts and some basaltic andesites that are consistent with crystal fractionation of olivine, plagioclase, and clinopyroxene as the melts evolve from 8.6 to about 5.4 wt % MgO. These follow a simple fractionation path consistent with MELTS modeling with decreasing Al_2O_3 and CaO, slightly increasing SiO_2, and increasing TiO_2, FeO, MnO, Na_2O, K_2O, P_2O_5, Cl, and S with decreasing MgO. The final part of the lava sequence starts at $\sim$2.5 wt % MgO and continues to near-zero MgO contents and encompasses some andesites, the dacites, and rhyolites. These variation trends are consistent with evolution by crystal fractionation of the crystals observed in the lavas: plagioclase, clinopyroxene, fayalitic olivine, titanomagnetite, and traces of apatite, zircon, pigeonite and orthopyroxene, and pyrite (Dreyer et al., 2017). The middle part consists of intermediate lavas having between 5 and 2.5% MgO that are basaltic andesites and andesites that do not follow liquid lines of descent as modeled here or by Wanless et al. (2012, their Figures 4 and 5). Their compositions are consistent with mixing (Dreyer et al., 2017) between basalt and dacite-to-rhyolite compositions (Figure 16) and almost all of these hybrids are located adjacent to and north of the rhyolite dome in AR6.

Hybridization also modifies the compositions of MORB in the northern part of AR6 and eastern PT (e.g., D747-R20, Figure 14). These modifications are much subtler, but result in higher SiO_2 and K_2O and lower TiO_2, FeO, and P_2O_5 (Figure 15) for most MORB on the eastern part of PT. Offsets are consistent with mixing or contaminating N-MORB with small amounts of silicic lava or melt that has crystallized Fe-Ti oxides and apatite, phases that constrain the silicic mixing component to be dacite to rhyolite. One of the most compelling changes this hybridization has on the composition of the basalt is to make it appear to be an E-MORB with $K_2O/TiO_2 > 0.2\%$ (Figure 17), by lowering TiO_2 and raising K_2O in the MORB.

The most extreme hybridization of MORB on the northern portion of AR6 is D740-R3 (Figure 16), which requires mixing between MORB with 7.5–8 wt % MgO and average rhyolite to average dacite. Mass balance calculations indicate mixing/assimilation of 10% rhyolite to 14% dacite to achieve the observed composition.

6.3. Subaxial Melt Migration

The generally decreasing MgO contents of MORB and decreasing occurrence of channelized flows with distance from the shallowest section of the ridge is consistent with upwelling of magma beneath the inflated and shallow AR2 and lateral transport and cooling in a subaxial magma lens along the ridge, as discussed in section 6.1.6. The hybridization discussed above in section 6.2.2 is consistent with melt being transported along axis past the cooling magma under the rhyolite dome, where the only highly evolved lavas on AR were erupted. At depth, silicic magmas/intrusions are available to contaminate later MORB melts over a zone about 1.6 km wide (from D740-R1 on NW side of axis to 12RC12 on SE side of axis), although 15RC3 (Figure 10) was not contaminated. Contaminated sample D740-R3 and less modified MORB D740-R1 are located $\sim$500 and 850 m west of the rhyolite dome, respectively (Figure 10), and D740-R3 postdates the rhyolite dome, the likely source of contamination, by about 2.2 ka. Most of the other slightly contaminated MORBs are located within 1 km east of the axial ridge and sampled during D742 and also erupted after the silicic lavas.

6.4. Transform Faults

6.4.1. Magmatism on Transform Faults

The concept of "leaky" transform faults was proposed as plate tectonic theory was being developed to explain how plate boundaries responded to changes in plate motion (Menard & Atwater, 1968). The Tamayo transform (Kastens et al., 1979; Macdonald et al., 1979) provided an early example of such a leaky transform based mainly on geophysical evidence for magma intrusion into a transform ridge. Bottom photographs from the deep-tow instrument package also showed some lava flows near the intersection of TT and the

EPR. Our mapping and sampling on TT and PT shows that channelized lava flows cover a high percentage of the mapped surface area and ages from the base of cores on top of these flows suggest the flows are younger than ~7.8 ka. Their morphology suggests they formed during high effusion rate eruptions (Gregg & Fink, 1995; Griffiths & Fink, 1992).

The sediment hills on TT and PT are similar morphologically to sediment hills uplifted by intrusion of sills in the Escanaba Trough on Gorda Ridge (Denlinger & Holmes, 1994; Morton & Fox, 1994). As observed here, in Escanaba Trough such hills host hydrothermal vent sites with heat derived from the sill that uplifted the sediment (Zierenberg et al., 1994). The lava flows on TT and PT can be traced uphill to the base of sediment hills, supporting the interpretation that the flows erupted from ring faults that surround uplifted sediment hills. In Escanaba Trough such ring faults surrounding sediment hills uplifted by emplacement of sills served as pathways for hydrothermal discharge and sulfide deposition (Denlinger & Holmes, 1994). Along the TT and PT, the ring faults around uplifted sediment hills not only served as conduits for hydrothermal fluids, but also for magma that erupted rapidly to feed lava to form channelized flows.

6.4.2. Melt Migration to the Transforms

There is evidence that the magmas intruded into the TT and PT were transported along the length of the ridge axis in a subaxial magma lens that bends around to the orientation of the transform faults. The lavas erupted along TT have lower MgO content, and were therefore cooler, than lavas erupted along AR1. At PT, the T-MORB lavas are also relatively low MgO, but not generally lower than the evolved lavas that dominate adjacent AR6. However, within approximately 5 km of the transform-ridge intersection the basalts are slightly contaminated by highly silicic magmas or country rock (Figure 14). This contamination of the eastern PT basalts by silicic compositions is consistent with their passage through the crust at AR6 after emplacement of the silicic lavas and around the bend into the transform fault. Western PT lavas are not similarly contaminated, suggesting that they might predate formation of highly evolved dacite and rhyolitic magmas on AR6, or their lateral or vertical migration avoided the AR6 zone of silicic magmas. The inferred minimum ages of the some of the western PT lavas of 4.8 ka, and the much older ages of silicic flows on AR6 of >11.7 ka argues against the idea that these lavas might predate the formation of the silicic magmas on AR6. The similar degree of fractionation of the eastern and western PT lavas suggests they had similar cooling histories and that both migrated along the ridge, with the western PT magmas avoiding subsurface interaction with silicic melts/intrusions under AR6. This avoidance might be related to depth of the dike, or a dike that followed other dikes that isolated it from the surrounding silicic melts or intrusions.

6.4.3. Tectonics on the Transforms

The magmatism mapped along TT and PT indicates that both transforms are transtensional to accommodate dike and sill emplacement. If the transforms had simple strike-slip motion, no accommodation space would exist for magma injection. Counterclockwise rotation of AR as the Gulf of California opens (e.g., Umhoefer, 2011) creates the transtensional environment.

Cores on top of two uplifted sediment hills with >50–70 m-thick unit of sandy silt is located where ocean crust younger than ~2.5 Ma occurs on the south side and ocean crust younger than a few hundred ka occurs on the north side of the transform (DeMets et al., 2010). The upper part of this sediment package yielded minimum ages of 17.9 and 17.7 ka. The sediment, because of its thickness and presence of abundant micas, botanical debris, and charcoal fragments, is tentatively inferred to be continentally derived although there is no direct connection to any continental source area. We hypothesize that the underlying >50–70 m of sediment was deposited on the margin of the Gulf near the southeast end of the TT as the Gulf rifted before 3.6 Ma (e.g., DeMets et al., 2010; Umhoefer, 2011). The transform ridges would be caught between two fault traces of the transform as the Gulf opened. The recovery of similar sandy silt on the PT requires a similar explanation.

6.5. Emplacement of Off-Axis Flows

Anomalously young off-axis lava flows have been attributed to off-axis eruptions (e.g., Reynolds & Langmuir, 2000; Sims et al., 2003) or to advance of flows away from the ridge axis where they erupted (e.g., Carbotte et al., 1997; Escartin et al., 2007; Fundis et al., 2010; Kurras et al., 2000; Macdonald et al., 1989; Sims et al., 2003, Soule et al., 2005, 2007, 2009; Waters et al., 2013). Most of these studies address how ocean crust is constructed, and the studies were done at fast spreading ridges. A number address how the roughly 2–3 km 2005–2006 lava flows at 9°N advanced off axis. Our data show that the same processes take place at intermediate-spreading rate ridges such as AR.

AR3 displays both types of off-axis flows (Figure 7). The large cone with deep crater is evidence of off-axis activity, otherwise the cone would have been split by subsequent spreading with remnants located NW and SE of the present axis. An example of such tectonic splitting of a cone occurs just west of the circular cone. A core from the bottom of the crater in the circular cone yielded a radiocarbon age of 12.0 ka compared to the predicted crustal age based on spreading rate and distance to the axis of ~140 ka (Figure 18). This age difference suggests the cone formed on ~128 ka-old ocean crust ~5.2 km west of the neovolcanic axis.

AR3 also has evidence of off-axis transport of channelized lava flows for distances of 3–4.5 km (Figure 18). The distance the flows extend off axis is similar in length to off-axis flows described by Waters et al. (2013) but greater than observed for other flows mapped on the EPR (e.g., Fundis et al., 2010; Soule et al., 2005, 2007, 2009). It still falls far short of the estimated 11 km off axis advance of the 220 km^2 flow at 8°S (Macdonald et al., 1989). As Escartin et al. (2007) and Le Saout et al. (2014) note, the advance of off-axis flows is stopped when they reach a fault too tall to overtop. The flows mapped on AR3 extend 3.5 km to the scarp at the base of the next older abyssal hill to the west, where the crustal age is inferred to be about 190 ka. Two of the channelized flows yielded core ages of 12.5 and 14 ka, suggesting that far-traveled younger flows are adding to the thickness of the layer 2A (extrusive volcanics) crust for ~175 ka.

7. Conclusions

A. Minimum axial depth, maximum lava temperatures, minimum lava flow ages, maximum lava effusion rates, and active (and inactive) hydrothermal vents are not located midway along the segment on the intermediate-spreading rate Alarcon Rise but on the most magmatically robust region, about 1/3 of the distance along the segment. The inflated portion of the axis is paved by a 16 km^2 channelized flow erupted from 9 km-long en echelon fissure system. This lava flow covers a larger area than any known historical lava flow on the EPR or Gorda and Juan de Fuca Ridges. The lavas are barely hotter than basalts erupted elsewhere along most of the ridge segment. The basalts along Alarcon Rise are mainly primitive (>8% MgO) N-MORB near the inflated part of the ridge, trending to a mix of more fractionated N-MORB and T-MORB nearer the transforms. A single flow of E-MORB occurs near the center of the segment but off axis and may represent a seldom-erupted compositional end member that mixes with N-MORB to form T-MORB.

B. Magmatism of Pescadero and Tamayo transforms occurs as sill injection in thick sediment, and eruption from ring-faults surrounding uplifted sediment hills above the sills to form extensive channelized flows. The transforms are transtensional to accommodate magma migration and emplacement. This transtensional regime probably results from rotation as the Gulf of California opens and may also be responsible for a 1 km shift in the location of the spreading axis to the SW.

C. Sediment on Tamayo and Pescadero transforms is thicker than the ~50–70 m full penetration of the chirp sonar with minimum ages at <1 m depth on the Tamayo transform of 18 kyrs. The ridge on Tamayo transform is a fault sliver of continental margin sediment, probably from the southeast end of the transform.

D. Basaltic andesite, andesite, dacite, and the first rhyolite sampled from the submarine global mid-ocean ridge system dominate the northern part of Alarcon Rise within ~17 km of the Pescadero transform with dacite and rhyolite between 5 and 10 km of the transform. Crystal fractionation, assimilation of Cl derived from seawater, and magma mixing all play roles in formation of the silicic lavas between 11.7 and 1.1 ka and in modifying basalts on the northern ridge and eastern Pescadero transform. Magma migrates laterally along not only the entire Alarcon Rise, but around the ridge-transform intersections into both transforms. Silicic lavas form closer to the adjacent Pescadero transform than at the tip of the 9°N overlapping spreading center, due to the enhanced cold-edge effect of the Pescadero transform which has continental crust within ~7 km of its north side.

E. A traverse away from the axis shows no systematic variations in magma compositions over about 13.7 kyr of activity. Off-axis lava consists of erupted off axis and channelized flows that traveled at least as far as 3.5 km from the inflated portion of the axis and emplaced across the entire valley NW of the axis.

Acknowledgments
A project of this scope is only possible with the enthusiastic and able help of many people. Primary among them are the captains and ship crews of the R/Vs *Western Flyer* (in 2003, 2012, and 2015), *Zephyr* (in 2012), and *Rachel Carson* (in 2015), the chief pilots and teams of ROVs *Tiburon* (in 2003) and *Doc Rickets* (in 2012 and 2015), and the technical team led by Hans Thomas for the AUV *D. Allan B.* (in 2012 and 2015), without whom none of the mapping data, observations or samples presented here would have been collected. At sea, we had the assistance of students Abigail Johnson, Christine A. Maschmeyer, Elias Meneses-Quiroz, Florian Neumann, Carolina Nieves-Cardoso, and Hiram Rivera-Huerta. On-shore, Greg Baxter made the polished glass grain-mounts and Nick Botto and Sarah Roeske assisted in analyzing the glasses by electron microprobe at UC Davis, Mary McGann of Diablo Geological Services picked the foraminifera for Thomas P. Guilderson to date using AMS at LLNL. The rock and core samples are curated at MBARI and the AUV mapping data is posted with IEDA. The project was supported by a grant from the David and Lucile Packard Foundation to MBARI, with postcruise NSF support for geochemical work from OCE-1355436 and OCE-1610800 to B.M.D. and R.A.P.

References

Byerly, G. R., Melson, W. G., & Vogt, P. R. (1976). Rhyodacites, andesites, ferrobasalts and ocean tholeiites from the Galapagos spreading center. *Earth and Planetary Science Letters*, *30*, 215–221.

Carbotte, S. M., & Macdonald, K. C. (1994). The axial topographic high at intermediate and fast spreading ridges. *Earth and Planetary Science Letters*, *128*, 85–97.

Carbotte, S. M., Mutter, J. C., & Xu, L. (1997). Contribution of volcanism and tectonism to axial and flank morphology of the southern East Pacific Rise, 7°10′–7°40′S, from a study of layer 2A geometry. *Journal of Geophysical Research*, *102*, 10165–10184.

Caress, D. W., & Chayes, D. N. (2010). *MB-System: Open source software for the processing and display of swath mapping sonar data*. Palisades, NY: Lamont-Doherty Earth Observatory of Columbia University. Retrieved from http://www.mbari.org/products/research-software/mb-system/

Caress, D., Clague, D., Paduan, J., Martin, J., Dreyer, B., Chadwick, W. W., Jr., et al. (2012). Repeat bathymetric surveys at 1-metre resolution of lava flows erupted at Axial Seamount in April 2011. *Nature Geoscience*, *5*(7), 483. https://doi.org/10.1038/ngeo1496

Caress, D., Paduan, J., Clague, D., & Spelz-Madero, R. (2018). *Processed gridded near-bottom bathymetry data (ArcASCII format) from the Alarcon Rise Spreading Center*. Integrated Earth Data Applications (IEDA). https://doi.org/10.1594/IEDA/324367

Caress, D. W., Thomas, H., Kirkwood, W. J., McEwen, R., Henthorn, R., Clague, D. A., et al. (2008). High-resolution multibeam, sidescan, and subbottom surveys using the MBARI AUV D. Allan B. In J. R. Reynolds & H. G. Greene (Eds.), *Marine habitat mapping technology for Alaska* (pp. 47–70). Fairbanks: University of Alaska Fairbanks. https://doi.org/10.4027/mhmta.2008.04

Caress, D., Troni, G., Clague, D. A., Paduan, J. B., Martin, J. F., Thomas, H. J., et al. (2015). *Detection of active hydrothermal vent fields in the Pescadero Basin and on the Alarcon Rise using AUV multibeam and CTD data*. Abstract OS23C-2027 presented at the American Geophysical Union Fall Meeting, San Francisco, December 14–18.

Castillo, P. R., Hawkins, J. W., Lonsdale, P. F., Hilton, D. R., Shaw, A. M., & Glascock, M. D. (2002). Petrology of Alarcon Rise lavas, Gulf of California: Nascent intracontinental ocean crust. *Journal of Geophysical Research*, *107*(B10), 2222. https://doi.org/10.1029/2001JB000666

Chadwick, W. W., Jr., Clague, D. A., Embley, R. W., Perfit, M. R., Butterfield, D. A., Caress, D. W., et al. (2013). The 1998 eruption of Axial Seamount: New insights on submarine lava flow emplacement from high-resolution mapping. *Geochemistry Geophysics Geosystems*, *14*, 3939–3968. https://doi.org/10.1002/ggge.20202

Christie, D., & Sinton, J. M. (1981). Evolution of abyssal lavas along propagating segments of the Galapagos spreading center. *Earth and Planetary Science Letters*, *56*, 321–335. https://doi.org/10.1016/0012-821X(81)90137-0

Clague, D. A., & Bunch, T. E. (1976). Formation of mid-ocean ridge ferrobasalt at east Pacific midocean ridge spreading centers. *Journal of Geophysical Research*, *81*, 4247–4256.

Clague, D. A., Dreyer, B. M., Paduan, J. B., Martin, J. F., Caress, D. W., Gill, J. B., et al. (2014). Eruptive and tectonic history of the Endeavour Segment, Juan de Fuca Ridge, based on AUV mapping data and lava flow ages. *Geochemistry, Geophysics, Geosystems*, *15*, 3364–3391. https://doi.org/10.1002/2014GC005415

Clague, D. A., Dreyer, B. M., Paduan, J. B., Martin, J. F., Chadwick, W. W., Jr., Caress, D. W., et al. (2013). Geologic history of the summit of Axial Seamount, Juan de Fuca Ridge. *Geochemistry Geophysics Geosystems*, *14*, 4403–4443. https://doi.org/10.1002/ggge.20240

Clague, D. A., Frey, F. A., Thompson, G., & Rindge, S. (1981). Trace element geochemistry of dredged volcanic rocks from the Galapagos Spreading Center: Role of crystal fractionation and mantle heterogeneity. *Journal of Geophysical Research*, *86*, 9469–9482.

Clague, D. A., & Paduan, J. B. (2009). Submarine basaltic volcanism. In B. Cousens & S. J. Piercey (Eds.), *Submarine volcanism and mineralization: Modern through ancient, Short course notes, Geological Society of Canada* (Vol. 19, pp. 41–60). St. John's, NL, Canada: Geological Association of Canada, Mineral Deposits Division.

Clague, D. A., Paduan, J. B., Caress, D. W., Chadwick, W. W., Jr., Le Saout, M., Dreyer, B., et al. (2017). High-resolution AUV mapping and targeted ROV observations of three historical lava flows at Axial Seamount. *Oceanography*, *30*(4). https://doi.org/10.5670/oceanog.2017.426

Clague, D. A., Paduan, J. B., & Davis, A. S. (2009). Widespread strombolian eruptions of mid-ocean ridge basalt. *Journal of Volcanology and Geothermal Research*, *180*(2–4), 171–188. https://doi.org/10.1016/j.jvolgeores.2008.08.007

Colman, A., Sinton, J., White, S. M., McClinton, J. T., Bowles, J. A., Rubin, K. H., et al. (2012). Effects of variable magma supply on mid-ocean ridge eruptions: Constraints from mapped lava flow fields along the Galápagos Spreading Center. *Geochemistry Geophysics Geosystems*, *13*, Q08014. https://doi.org/10.1029/2012GC004163

Cox, K. G., Bell, J. D., & Pankhurst, R. J. (1979). *The interpretation of igneous rocks* (450 pp.). London, UK: Allen and Unwin.

DeMets, C., Gordon, R. G., & Argus, D. F. (2010). Geologically current plate motions. *Geophysical Journal International*, *181*, 1–80.

Denlinger, R. P., & Holmes, M. L. (1994). A thermal and mechanical model for sediment hills and associated sulfide deposits along the Escanaba Trough. In J. L Morton, R. A. Zierenberg, & C. A. Reiss (Eds.), *Geologic, hydrothermal, and biologic studies at Escanaba Trough, Gorda Ridge, offshore northern California* (U.S. Geol. Surv. Bull. 2022, chap. 4, pp. 65–76).

Dreyer, B. M., Portner, R. A., & Clague, D. A. (2017). *Mixing and hybridization in basalt-to-rhyolite magmatism on an intermediate spreading mid-ocean ridge, Alarcon Rise, EPR*. Abstract presented at the Chapman Conference on Submarine Volcanism, Hobart, Australia, January 30 to February 3, 2017.

Dreyer, B. M., Portner, R. A., Clague, D. A., Castillo, P. R., Paduan, J. B., & Martin, J. F. (2012). *Rhyolite, dacite, andesite, basaltic andesite, and basalt volcanism on the Alarcón Rise spreading-center, Gulf of California*. Abstract T51B-2570 presented at the American Geophysical Union Fall Meeting, San Francisco, CA, December 3–7.

Escartin, J., Soule, S. A., Fornari, D. J., Tivey, M. A., Schouten, H., & Perfit, M. R. (2007). Interplay between faults and lava flows in construction of the upper oceanic crust: The East Pacific Rise crest 9°25′–9°. *Geochemistry Geophysics Geosystems*, *8*, Q06005. https://doi.org/10.1029/2006GC001399

Ferrini, V. L., Fornari, D. J., Shank, T. M., Kinsey, J. C., Tivey, M. A., Soule, S. A., et al. (2007). Submeter bathymetric mapping of volcanic and hydrothermal features on the East Pacific Rise crest at 9°50′N. *Geochemistry Geophysics Geosystems*, *8*, Q01006. https://doi.org/10.1029/2006GC001333

Fornari, D. J., Tivey, M. A., Schouten, H., Perfit, M. R., Yoerger, D., Bradley, A., et al. (2004). Submarine lava flow emplacement at the East Pacific Rise 9°50′N: Implications for uppermost ocean crust stratigraphy and hydrothermal fluid circulation. In C. R. German, J. Lin, & L. M. Parson (Eds.), *Mid-ocean ridges: Hydrothermal interactions between the lithosphere and oceans, Geophysical monograph series* (Vol. 148, pp. 187–218). Washington, DC: American Geophysical Union.

Fornari, D. J., Von Damm, K. L., Bryce, J. G., Cowen, J. P., Ferrini, V., Fundis, A., et al. (2012). The East Pacific Rise between 9°N and 10°N: Twenty-five years of integrated, multidisciplinary oceanic spreading center studies. *Oceanography*, *25*(1), 18–43. https://doi.org/10.5670/oceanog.2012.02

Freund, S., Beier, C., Krumm, S., & Haase, K. M. (2013). Oxygen isotope evidence for the formation of andesite-daciic magmas from the fast-spreading Pacific-Antarctic Rise by assimilation-fractional crystallization. *Chemical Geology*, *347*, 271–283.

Fundis, A. T., Soule, S., Fornari, D. J., & Perfit, M. R. (2010). Paving the seafloor: Volcanic emplacement processes during the 2005–2006 eruptions at the fast spreading East Pacific Rise, 9°. *Geochemistry Geophysics Geosystems*, *11*, Q08024. https://doi.org/10.1029/2010GC003058

Ghiorso, M. S., & Sack, R. O. (1995). Chemical mass transfer in magmatic processes IV. A revised and internally consistent thermodynamic model for the interpolation and extrapolation of liquid-solid equilibria in magmatic systems at elevated temperatures and pressures. *Contributions to Mineralogy and Petrology*, *119*(2–3), 197–212.

Goffredi, S., Johnson, S., Tunnicliffe, V., Caress, D., Clague, D., Escobar, E., et al. (2017). Hydrothermal vent fields discovered in southern Gulf of California clarify role of habitat in augmenting regional diversity. *Proceedings of the Royal Society B*, *284*, 20170817. https://doi.org/10.1098/rspb.2017.0817

Goss, A. R., Perfit, M. R., Ridley, W. I., Rubin, K. H., Kamenov, G. D., Soule, S. A., et al. (2010). Geochemistry of lavas from the 2005–2006 eruption at the East Pacific Rise, 9°46′N–9°56′N: Implications for ridge crest plumbing and decadal changes in magma chamber compositions. *Geochemistry Geophysics Geosystems*, *11*, Q05T09. https://doi.org/10.1029/2009GC002977

Gregg, T. K. P., & Fink, J. H. (1995). Quantification of submarine lava-flow morphology through analog experiments. *Geology*, *23*(1), 73–76.

Griffiths, R. W., & Fink, J. H. (1992). Solidification and morphology of submarine lavas: A dependence on extrusion rate. *Journal of Geophysical Research*, *97*, 19729–19737.

Gualda, G. A. R., Ghiorso, M. S., Lemons, R. V., & Carley, T. L. (2012). Rhyolite-MELTS: A modified calibration of MELTS optimized for silica-rich, fluid-bearing magmatic systems. *Journal of Petrology*, *53*, 875–890. https://doi.org/10.1093/petrology/egr080

Haymon, R., Fornari, D., Edwards, M., Carbotte, S., Wright, D., & Macdonald, K. (1991). Hydrothermal vent distribution along the East Pacific Rise crest (9°09′′–54′′N) and its relationship to magmatic and tectonic processes on fast-spreading mid-ocean ridges. *Earth and Planetary Science Letters*, *104*(2–4), 513–534. https://doi.org/10.1016/0012-821X(91)90226-8

Jamieson, J. W., Clague, D. A., & Hannington, M. D. (2014). Hydrothermal sulfide accumulation along the Endeavour Segment segment, Juan de Fuca Ridge. *Earth Planetary Science Letters*, *395*, 136–148. https://doi.org/10.1016/j.epsl.2014.03.035

Jamieson, J. W., Hannington, M. D., Clague, D. A., Kelley, D. S., Delaney, J. R., Holden, J. F., et al. (2013). Sulfide geochronology along the Endeavour Segment of the Juan de Fuca Ridge. *Geochemistry, Geophysics, Geosystems*, *14*, 2084–2099. https://doi.org/10.1002/ggge.20133

Kappel, E. S., & Ryan, W. B. F. (1986). Volcanic episodicity and a non-steady state rift valley along northeast Pacific spreading centers: Evidence from Sea MARC I. *Journal of Geophysical Research*, *91*, 13925–13940. https://doi.org/10.1029/JB091iB14p13925

Kastens, K. A., Macdonald, K. C., & Becker, K. (1979). The Tamayo transform fault in the mouth of the Gulf of California. *Marine Geophysical Researches*, *4*, 129–151.

Kurras, G. J., Fornari, D. J., Edwards, M. H., Perfit, M. R., & Smith, M. C. (2000). Volcanic morphology of the East Pacific Rise crest 9°49–52′: Implications for volcanic emplacement processes at fast-spreading mid-ocean ridges. *Marine Geophysical Researches*, *21*, 23–41.

Langmuir, C. H., Bender, J. F., & Batiza, R. (1986). Petrological and tectonic segmentation of the East Pacific Rise 5°30′N–14°30′N. *Nature*, *322*, 422–429.

Le Saout, M., Clague, D. A., Paduan, J. B., & Caress, D. W. (2016). *Evolution of fine-scale segmentation at intermediate ridges: Examples of Alarcon Rise and Endeavour segment*, Abstract OS31D-2066 presented at the American Geophysical Union Fall Meeting, San Francisco, CA, December 12–16.

Le Saout, M., Deschamps, A., Soule, S. A., & Gente, P. (2014). Segmentation and eruptive activity along the East Pacific Rise at 16°N, in relation with the nearby Mathematician hotspot. *Geochemistry, Geophysics, Geosystems*, *15*, 4380–4399. https://doi.org/10.1002/2014GC005560

Lizarralde, D., Axen, G. J., Brown, H. E., Fletcher, J. M., González-Fernández, A., Harding, A. J., et al. (2007). Variations in styles of rifting in the Gulf of California. *Nature*, *448*(7152), 466–469. https://doi.org/10.1038/nature06035

Lonsdale, P. (1989). Segmentation of the Pacific-Nazca spreading center, 1°N–20°S. *Journal of Geophysical Research*, *94*, 12197–12225.

Macdonald, K. C. (1998). Linkages between faulting, volcanism, hydrothermal activity and segmentation on fast-spreading centers. In W. R. Buck et al. (Eds.), *Faulting and magmatism at mid-ocean ridges, Geophysical monograph series* (Vol. 106, pp. 27–58). Washington, DC: AGU.

Macdonald, K. C., Haymon, R., & Shor, A. (1989). A 220 km^2 recently erupted lava field on the East Pacific Rise near lat 8°S. *Geology*, *17*, 212–216.

Macdonald, K. C., Kastens, K., Spiess, F. N., & Miller, S. P. (1979). Deep-tow studies of the Tamayo transform fault. *Marine Geophysical Researches*, *4*(1), 37–70.

Macdonald, K. C., Scheirer, D. S., & Carbotte, S. M. (1991). Mid-ocean ridges: Discontinuities, segments, and giant cracks. *Science*, *253*, 986–994.

Macdonald, K. C., Sempere, J.-C., & Fox, P. J. (1984). East Pacific Rise from Siqueros to Orozco Fracture Zones: Along-strike continuity of axial neovolcanic zone and structure and evolution of overlapping spreading centers. *Journal of Geophysical Research*, *89*, 6049–6069.

Martin, J. F., Clark, P. L., Clague, D. A., Caress, D. W., Portner, R. A., Paduan, J. B., et al. (2012). *Effect of melt composition and crystal content on flow morphology along the Alarcón Rise, Mexico.* Abstract T51B-2571 presented at the Fall AGU Meeting, San Francisco, CA, December 3–7.

Maschmeyer, C., White, S., Dreyer, B., & Clague, D. A. (2015). *Detection of high-silica lava flows and lava morphology at the Alarcon Rise, Gulf of California, Mexico using automated classification of the morphological-compositional relationship in AUV multibeam bathymetry and sonar backscatter*. Abstract OS23C-2032 presented at the American Geophysical Union Fall Meeting, San Francisco, CA, December 14–18.

Menard, H. W., & Atwater, T. M. (1968). Changes in directions of seafloor spreading. *Nature*, *219*, 463–467.

Morton, J. L., & Fox, C. G. (1994). Structural setting and interaction of volcanism and sedimentation at Escanaba Trough: Geophysical results. In J. L. Morton, R. A. Zierenberg, & C. A. Reiss (Eds.), *Geologic, hydrothermal, and biologic studies at Escanaba Trough, Gorda Ridge, offshore northern California* (U.S. Geol. Surv. Bull. 2022, chap. 2, pp. 21–43).

Paduan, J. B., Clague, D. A., Caress, D. W., Lundsten, L., Martin, J. F., & Nieves-Cardoso, C. (2012). *Newly discovered hydrothermal system on the Alarcón Rise, Mexico*. Abstract T51B-2572 presented at the Fall AGU Meeting, San Francisco, CA, December 3–7.

Paduan, J. B., Clague, D. A., Caress, D., Lundsten, L., Zierenberg, R., Troni, G., et al. (2015). *Seafloor hydrothermal activity in the southern Gulf of California*. Abstract OS22C-03 presented at the American Geophysical Union Fall Meeting, San Francisco, CA, December 14–18.

Perfit, M., & Fornari, D. (1983). Geochemical studies of abyssal lavas recovered by DSRV *Alvin* from Eastern Galapagos Rift, Inca transform, and Ecuador Rift: 2. Phase chemistry and crystallization history. *Journal of Geophysical Research*, *88*, 10530–10550. https://doi.org/10.1029/JB088iB12p10530

Perfit, M. R., & Chadwick, W. W., Jr. (1998). Magmatism at mid-ocean ridges: Constraints from volcanological and geochemical investigations. In W. R. Buck (Ed.), *Faulting and magmatism at mid-ocean ridges, Geophysical monograph series* (vol. 106, pp. 59–115). Washington, DC: AGU.

Portner, R. A., Dreyer, B. M., Clague, D. A., Lowernstern, J. B., Head, J. W., III, & Saal, A. (2014). *Degassing history of a mid-ocean ridge rhyolite dome on the Alarcon Rise, Gulf of California*. Abstract V11C-4735 presented at the American Geophysical Union Fall Meeting, San Francisco, CA, December 15–19.

Portner, R. A., Dreyer, B. M., Clague, D. A., Spelz, R., Lowernstern, J. B., Paduan, J. B., et al. (2015). *Rhyolite eruption on a mid-ocean ridge: Alarcon Rise, Gulf of California*. Paper presented at the Geological Society of America Annual Meeting, Abstracts with programs (Vol. 47, No. 7, p. 380), Baltimore, MD, November 1–4.

Regelous, M., Niu, Y. L., Wendt, J. I., Batiza, R., Greig, A., & Collerson, K. D. (1999). Variations in the geochemistry of magmatism on the East Pacific Rise at 10°30′N since 800 ka. *Earth and Planetary Science Letters*, *168*(1–2), 45–63. https://doi.org/10.1016/S0012-821X(99)00048-5

Reynolds, J. R., & Langmuir, C. H. (2000). Identification and implications of off-axis lava flows around the East Pacific Rise. *Geochemistry Geophysics Geosystems*, *1*(6), 1019. https://doi.org/10.1029/1999GC000033

Rubin, K. H., Smith, M. C., Bergmanis, E. C., Perfit, M. R., Sinton, J. M., & Batiza, R. (2001). Geochemical heterogeneity within mid-ocean ridge lava flows: Insights into eruption, emplacement and global variations in magma generation. *Earth and Planetary Science Letters*, *188*, 349–367.

Schmitt, A. K., Perfit, M. R., Rubin, K. H., Stockli, D. F., Smith, M. C., Cotsonika, L. A., et al. (2011). Rapid cooling rates at an active mid-ocean ridge from zircon thermochronology. *Earth and Planetary Science Letters*, *302*, 349–358.

Shorttle, O., Rudge, J. F., Maclennan, J., & Rubin, K. H. (2016). A statistical description of concurrent mixing and crystallization during MORB differentiation: Implications for trace element enrichment. *Journal of Petrology*, *57*(11–12), 2127–2162.

Sims, K. W. W., Blichert-Toft, J., Fornari, D. J., Perfit, M. R., Goldstein, S. J., Johnson, P., et al. (2003). Aberrant youth: Chemical and isotopic constraints on the origin of off-axis lavas from the East Pacific Rise 9°–10°SN. *Geochemistry Geophysics Geosystems*, *4*(10), 8621. https://doi.org/10.1029/2002GC000443

Sinton, J. M., Wilson, D. S., Christie, D. M., Hey, R. N., & Delaney, J. R. (1983). Petrologic consequences of rift propagation on oceanic spreading ridges. *Earth and Planetary Science Letters*, *62*(2), 193–207. https://doi.org/10.1016/0012-821X(83)90083-3

Smith, P. M., & Asimow, P. D. (2005). Adiabat_1ph: A new public front-end to the MELTS, pMELTS, and phMELTS models. *Geochemistry, Geophysics, Geosystems*, *6*, Q02004. https://doi.org/10.1029/2004GC000816

Soule, S. A., Escartín, J., & Fornari, D. J. (2009). A record of eruption and intrusion at a fast spreading ridge axis: Axial summit trough of the East Pacific Rise at 9–10°N. *Geochemistry Geophysics Geosystems*, *10*, Q10T07. https://doi.org/10.1029/2008GC002354

Soule, S. A., Fornari, D. J., Perfit, M. R., & Rubin, K. H. (2007). New insights into mid-ocean ridge volcanic processes from the 2005–2006 eruption of the East Pacific Rise, 9°46′N–9°56′N. *Geology*, *35*(12), 1079–1082. https://doi.org/10.1130/G23924A.1

Soule, S. A., Fornari, D. J., Perfit, M. R., Tivey, M. A., Ridley, W. I., & Schouten, H. (2005). Channelized lava flows at the East Pacific Rise crest 9°–10°N: The importance of off-axis lava transport in developing the architecture of young oceanic crust. *Geochemistry Geophysics Geosystems*, *6*, Q08005. https://doi.org/10.1029/2005GC000912

Spelz, R. M., Fletcher, J. M., Nieves-Cardoso, C., Santa Rosa-del Rio, M., Caress, D. W., Clague, D. A., et al. (2012). *The Alarcón Rise: Detail mapping and preliminary results on the geometry, distribution and kinematics of faults and fissures on a ridge-transform system*. Abstract T51B-2567 presented at the Fall AGU Meeting, San Francisco, CA, December 3–7.

Stakes, D. S., Perfit, M. R., Tivey, M. A., Caress, D. W., Ramirez, T. M., & Maher, N. (2006). The Cleft revealed: Geologic, magnetic, and morphologic evidence for construction of the upper oceanic crust along the southern Juan de Fuca Ridge. *Geochemistry Geophysics Geosystems*, *7*, Q04003. https://doi.org/10.1029/2005GC001038

Stuiver, M., & Reimer, P. J. (1993). Extended 14C data base and revised CALIB 3.0 14C age calibration programme. *Radiocarbon*, *35*(1), 215–231.

Toomey, D. R., & Hooft, E. E. E. (2008). Mantle upwelling, magmatic differentiation, and the meaning of axial depth at fast-spreading ridges. *Geology*, *36*(9), 679–692. https://doi.org/10.1130/G24834A.1

Umhoefer, P. J. (2011). Why did the southern Gulf of California rupture so rapidly?—Oblique divergence across a hot, weak lithosphere along a tectonically active margin. *GSA Today*, *21*(11), 4–10. https://doi.org/10.1130/G133A.1

Wanless, V. D., Perfit, M. R., Klein, E. M., White, S., & Ridley, W. I. (2012). Reconciling geochemical and geophysical observations of magma supply and melt distribution at the 9°N overlapping spreading center, East Pacific Rise. *Geochemistry Geophysics Geosystems*, *13*, Q11005. https://doi.org/10.1029/2012GC004168

Wanless, V. D., Perfit, M. R., Ridley, W. I., & Klein, E. (2010). Dacite petrogenesis on mid-ocean ridges: Evidence for oceanic crustal melting and assimilation. *Journal of Petrology*, *51*(12), 2377–2410. https://doi.org/10.1093/petrology/egq056

Wanless, V. D., Perfit, M. R., Ridley, W. I., Wallace, P. J., Grimes, C. B., & Klein, E. M. (2011). Volatile abundances and oxygen isotopes in basaltic to dacitic lavas on mid-ocean ridges: The role of assimilation at spreading centers. *Chemical Geology*, *287*(1–2), 54–65. https://doi.org/10.1016/j.chemgeo.2011.05.017

Waters, C. L., Sims, K. W. W., Soule, S. A., Blichert-Toft, J., Dunbar, N. W., Plank, T., et al. (2013). Recent volcanic accretion at 9°N–10°N East Pacific Rise as resolved by combined geochemical and geological observations. *Geochemistry Geophysics Geosystems*, *14*, 2547–2574. https://doi.org/10.1002/ggge.20134

Wetzel, A., Werner, F., & Stow, D. A. V. (2008). Chapter 11 Bioturbation and biogentic sedimentary structures in contourites. *Developments in Sedimentology*, *60*, 183–202.

White, S. M., Haymon, R. M., Fornari, D. J., Perfit, M. R., & Macdonald, K. C. (2002). Correlation between volcanic and tectonic segmentation of fast-spreading ridges: Evidence from volcanic structures and lava morphology on the East Pacific Rise, 9°–10°N. *Journal of Geophysical Research*, *107*(B8), 2173. https://doi.org/10.1029/2001JB000571

White, S. M., Macdonald, K. C., & Haymon, R. M. (2000). Basaltic lava domes, lava lakes, and volcanic segmentation on the southern East Pacific Rise. *Journal of Geophysical Research*, *105*, 23519–23536. https://doi.org/10.1029/2000JB900248

Yeo, I. A., Clague, D. A., Martin, J. F., Paduan, J. B., & Caress, D. W. (2013). Pre-eruptive flow focusing in dikes feeding historical pillow ridges on the Juan de Fuca and Gorda Ridges. *Geochemistry Geophysics Geosystems*, *14*, 3586–3599. https://doi.org/10.1002/ggge.20210

Zierenberg, R. A., Morton, J. L., Koski, R. A., & Ross, S. L. (1994). Geologic setting of massive sulfide mineralization in the Escanaba Trough. In J. L. Morton, R. A. Zierenberg, & C. A. Reiss (Eds.), *Geologic, hydrothermal, and biologic studies at Escanaba Trough, Gorda Ridge, offshore northern California* (U.S. Geol. Surv. Bull. 2022, chap. 10, pp. 201–221).